MOVING DIPOLAR FEATURES IN AN EMERGING FLUX REGION

P.N. BERNASCONI, D.M. RUST, M.K. GEORGOULIS, and
B.J. LABONTE
*JHU / Applied Physics Laboratory, 11100 John Hopkins Road, Laurel,
MD 20723-6099, USA*

Abstract. Using the Flare Genesis Experiment (FGE), a balloon-borne observatory with an 80-cm solar telescope, we observed the active region NOAA 8844 on January 25, 2000 for several hours. FGE was equipped with a vector polarimeter and a tunable Fabry-Pérot narrow-band filter. It recorded time series of filtergrams, vector magnetograms, and Dopplergrams at the Ca I 6122.2 Å line, and Hα filtergrams with a cadence between 2.5 and 7.5 minutes. At the time of the observations, NOAA 8844 was located at approximately 5°N 30°W. The region was rapidly growing during the observations; new magnetic flux was constantly emerging in three supergranules near its center. We describe in detail how the FGE data were analyzed and report on the structure and behavior of peculiar moving dipolar features (MDFs) observed in the active region. In longitudinal magnetograms, the MDFs appeared to be small dipoles in the emerging fields. The east-west orientation of their polarities was opposite that of the sunspots. The dipoles were oriented parallel to their direction of motion, which was in most cases towards the sunspots. Previously, dipolar moving magnetic features have only been observed flowing out from sunspots. Vector magnetograms show that the magnetic field of each MDF negative part was less inclined to the local horizontal than the ones of the positive part. We identify the MDFs as undulations, or stitches, where the emerging flux ropes are still tied to the photosphere. We present a U-loop model that can account for their unusual structure and behavior, and it shows how emerging flux can shed its entrained mass.

Key words: Sun – Active Regions – Magnetic fields – Flux emergence – Polarimetry

1. Introduction

Drawing on high-resolution vector magnetograms and Dopplergrams from the Flare Genesis Experiment (FGE) (Bernasconi *et al.*, 2000; 2001), we report here on dipolar moving magnetic features that appear *when flux is emerging* and coalescing to form sunspots. Although it is common to see unipolar magnetic features flowing into growing sunspots (Strous *et al.*, 1996; Strous and Zwaan, 1999), we believe this is the first time that moving dipolar features have been reported in a sunspot formation region. Hereafter we will call these features moving dipolar features or MDFs, to distinguish them from the moving magnetic features (MMFs) previously observed in sunspot decay.

Sheeley (1969) first reported the MMFs that flow outward from mature sunspots, and Harvey and Harvey (1973) first described their magnetic properties. MMFs are about 1000 km in diameter and move about 1 km/s from a spot radially across its moat (Brickhouse and LaBonte, 1988) to collect in a ring of magnetic flux fragments surrounding the spot. In maps of the longitudinal magnetic fields, MMFs appear as either single poles or dipoles (Shine and Title, 2001). They appear to be an important mechanism of sunspot decay. No detailed explanation of the MMF phenomenon is established, but most observations are consistent with the 'sea serpent' cartoon drawn by Harvey and Harvey (1973). In their article they suppose that discrete magnetic flux ropes are drawn away from the spot in partially submerged folds through mass motions originating in the Evershed flows of the penumbra.

Nye, Thomas and Cram (1984) observed an MMF having a 400 m/s downflow, and we will see that downflow is a common feature in the *sunspot-building* moving dipolar features described in the present paper. The magnetic field intensity in MMFs has not been well established because of their small size, but the vector magnetic field observations reported here clarify why this is so.

The FGE vector magnetograms reveal that the fields in MDFs are mostly horizontal and that they probably are areas where emerging flux ropes are stitched into the photosphere. That is, they appear to be U-loops (Spruit, Title, and van Ballegooijen, 1987), not the Ω-loops usually associated with flux emergence (Parker, 1994).

This paper is based on observations obtained during the Flare Genesis Experiment flight, which is described in Section 2 along with a summary of our data analysis techniques (Section 3). Readers most interested in the observations of MDFs in the emerging active region, NOAA 8844, should turn immediately to Section 4. We present our summary and conclusions in Section 5. The interesting relationships linking the emerging flux with the arch filament system seen in the chromosphere and with the X-ray and EUV structure of the overlying corona will be treated in another article (Schmieder *et al.*, 2002). Georgoulis *et al.* (2002) present a statistical analysis of the over 300 Ellerman bombs that we recorded in NOAA 8844.

2. Instrumentation

The Flare Genesis observations were obtained on January 10 – 27, 2000, during the FGE's second Antarctic flight (Bernasconi *et al.*, 1999; 2000). The principal element of the FGE is an 80-cm Cassegrain telescope with an F/1.5 ultra-low-expansion glass primary mirror and a crystalline silicon secondary mirror. The silicon efficiently conducts the heat, which is intense on the secondary mirror, into a thermal sink. Silicon also has low thermal distortion, so we believe the thermal distortion of the optics during the flight was negligible.

A helium-filled balloon, provided by the NASA Scientific Ballooning Facility, carried the FGE to an altitude of 37 km where it could view the sun 24 hours/day without clouds or image distortion by atmospheric turbulence. Bernasconi *et al.* (2000) describe the focal plane instrumentation in detail, but in brief, it consisted of a polarization analyzer unit (two liquid-crystal variable retarders and a linear polarizing filter), a selection of 1.25 Å order-isolation filters, a 0.16 Å tunable Fabry-Pérot etalon filter (Rust, 1994), refractive optics to present a 160" ∅ section of the Sun to a 1024 x 1024-pixel CCD electronic camera. The plate scale was 0.091" per pixel, and the image quality achieved was 0.5". We made observations of all four Stokes parameters in the red and blue wings of the Ca I line at 6122.2 Å. Unpolarized observations were obtained at 0.8 Å in the blue wing of the Hα line at 6562.8 Å. The Ca I observations yielded vector magnetograms, Dopplergrams and photospheric images. The Hα – 0.8 Å images recorded activity in the lower chromosphere and in the arch filament system in the corona.

3. Data acquisition and reduction

We selected the Ca I 6122.2 Å line to derive the vector magnetograms because the 0.16 Å bandpass of our Fabry-Pérot etalon provides the best signal-to-noise performance with such a broad line. However, with an effective Landé factor of only 1.75, the line is only moderately sensitive to Zeeman splitting.

The Stokes parameters were obtained from sequentially recorded sets of 12 filtergrams at the polarization states $I+Q$, $I-Q$, $I+U$, $I-U$, $I+V$, and $I-V$, at ± 0.08 Å in the wings of the Ca I line. The integration time for each filtergram was 30 ms. Approximately 130 s were needed to acquire and store the full set of vector polarimetric measurements (12 images). Following two such sets, a series of 12 chromospheric filtergrams was recorded. For these, the Fabry-Pérot passband was in the blue wing of Hα, – 0.8 Å off-band, and the integration time was 125 ms. Each sequence of two Ca I vector polarimetric sets and Hα observations required about 7.5 minutes. The sequence ran repeatedly for about 3.5 hours (from 15:50 UT to 19:16 UT on January 25, 2000). A total of 56 vector polarimetric sets and 324 chromospheric filtergrams were recorded.

3.1. BASIC DATA REDUCTION

The raw images were first corrected for camera dark-current offsets and then flat-fielded to account for pixel-to-pixel gain variations introduced by the camera electronics and optical system imperfections. To improve the signal-to-noise ratio, we resized the images to 512 × 512 pixels with a scale of 0.18" per pixel, corresponding to a field of view of 92.2" × 92.2" (66.3 × 66.3 Mm). We then carefully co-aligned the images to account for image motions caused by the residual telescope pointing errors and drifts.

The telescope telemetry did not provide a high-precision position in latitude and longitude of the region observed. We determined its precise location by comparing a longitudinal magnetogram acquired by FGE at 16:44 UT on January 25, 2000 with a Kitt Peak synoptic magnetogram recorded between 16:21 UT and 17:16 UT of the same day.

3.2. VECTOR MAGNETOGRAMS

We obtained Stokes images, Q/I, U/I, and V/I, by calculating the normalized difference between measurements of opposite polarization states. For example:

$$V/I = [(I+V) - (I-V)] \,/\, [(I+V) + (I-V)]. \tag{1}$$

The magnetic field components longitudinal ($B_{//}$) and transversal ($B_{\perp}$) to the line-of-sight direction (LOS) were calculated following Ronan, Mickey, and Orrall (1987):

$$B_{//} = L(\mathrm{V}/I), \qquad B_{\perp} = T\sqrt[4]{(Q/I)^2 + (U/I)^2}\,, \tag{2}$$

where L and T are two constants that depend on the magnetic sensitivity of the spectral line used, on the exact location of the Fabry-Pérot passband, and on the instrument polarimetric efficiency. We derived L and T by comparing the FGE data with vector magnetograms obtained by the

Imaging Vector Magnetograph (IVM) of Hawaii (Mickey *et al.*, 1996), which was observing the active region at the same time. The IVM has a lower spatial resolution than FGE but it records full Stokes profiles, and the longitudinal and transversal field components are derived by means of an inversion code that fits the Stokes profiles. The advantage of comparing the FGE vector polarimetric measurements with the IVM inverted vector magnetic data is that we do not risk overestimating or underestimating the effective magnetic field strength in either $B_{//}$ or $B_{\perp}$. Before comparing the two data sets, we resized, rotated, and co-aligned the FGE vector magnetograms to match the IVM resolution and field of view. From the comparison we derived the following calibration factors: $L = 26100 \pm 450$ Gauss, $T = 4500 \pm 100$ Gauss.

The magnetic field zenith angle γ, i.e. the vector field inclination with respect to the LOS, and azimuth χ were calculated, again following Ronan, Mickey, and Orrall (1987), as follows:

$$\gamma = \arctan\left({}^{B_{//}}\!\big/_{B_{\perp}} \right), \qquad \chi = \frac{1}{2}\arctan\left({}^{U/I}\!\big/_{Q/I} \right). \tag{3}$$

Because of the symmetry properties of the transverse Zeeman effect, another possible solution for the azimuth angle is: $\chi_1 = \chi + 180°$. This 180° ambiguity is not easily resolved. Many techniques have been proposed (see Metcalf, 1994 and references therein, as well as Skumanich and Semel, 1996). However, most techniques work well only for active regions that do not deviate too much from a potential field configuration. Active region NOAA 8844 contained several areas where the field structure was highly complex and non-potential. A totally automated algorithm would not be able to properly resolve the 180° ambiguity for those areas.

We adopted an approach that combines a potential field solution with an empirical estimate of the correct field orientation based on simple geometrical considerations. Out of the 56 recorded vector magnetograms, we selected one, which was kept as reference, and we resolved the 180° ambiguity for it. Initially, we compared the field vectors with a simple potential-field model derived from the longitudinal magnetogram. In this model we just considered the two main polarities in the active region and neglected the magnetic flux between them. We chose the field azimuths that minimized the angular difference with the model azimuths. The resulting vector magnetogram was subsequently filtered with a "smoothing algorithm" that checks for maximum continuity between adjacent vectors to create a smooth azimuthal distribution of vectors across the entire region. We then visually inspected the azimuth map and corrected manually any local geometrical inconsistencies. The vector field map was then transformed from the LOS reference system to the local, heliographic reference system. In the local reference system the zenith angle is expressed with respect to the local vertical and the azimuth with respect to the local *N-S*/*E-W* directions. The transformation into the heliographic reference system was helpful in revealing vectors that were incorrectly chosen due to the ≈ 30° off vertical viewing angle of the region in the LOS system. See Gary and Hagyard (1990) for a discussion on the effects of perspective. The transformed vector magnetogram was again visually inspected and corrected for local geometrical inconsistencies. We corrected the rest of the vector magnetograms sequentially by comparison with the preceding vector magnetograms, starting with the reference one. We assumed that the vector directions changed less than 90° during the times between consecutive magnetograms. After the sequential comparison procedure, a few vector magnetograms still needed some manual correction to account for isolated local errors.

Despite all our efforts to solve the 180° ambiguity problem, we still can not be completely sure that we chose the right solution across the entire field of view and for all 56 frames. However we believe that at worst, the ambiguity was incorrectly resolved only in a few isolated areas.

3.3. PHOTOSPHERIC DOPPLER MAPS

We derived photospheric Dopplergrams by calculating the normalized difference between filtergrams recorded in the two wings of the Ca I line. We averaged all the images recorded in each wing during each 12-image set and over two consecutive sets:

$$D_{\mathrm{b}} = \left(Q_b^+ + Q_b^- + U_b^+ + U_b^- + V_b^+ + V_b^-\right)_{\mathrm{set\,1}} + (\cdots)_{\mathrm{set\,2}}, \tag{4}$$

$$D_{\mathrm{r}} = \left(Q_r^+ + Q_r^- + U_r^+ + U_r^- + V_r^+ + V_r^-\right)_{\mathrm{set1}} + (\cdots)_{\mathrm{set\,2}}, \tag{5}$$

where the indices ‘b’ and ‘r’ mean blue and red wing, respectively. This was done to improve the signal-to-noise ratio, to remove some of the 5-min oscillations effects, and to cancel out image-to-image intensity variations introduced by the vector polarimetric measurements. The Doppler image was obtained as follows:

$$D = (D_{\mathrm{b}} - D_{\mathrm{r}}) / (D_{\mathrm{b}} + D_{\mathrm{r}}). \tag{6}$$

A positive value in D corresponds to a red shift in the line. To further reduce/remove 5-min oscillation effects and to reduce image-to-image noise, we applied a space-time Fourier filter. The filter combined a high-pass filter, for the noise, with a bandpass filter, for the intensity oscillations. The final time series consists of 28 Doppler images with a time step of approximately 7.5 minutes.

Each Doppler image D is just a map of the intensity difference between the blue and the red wings of the Ca I line. To estimate the longitudinal velocities V in the photosphere, we assumed a linear relationship between D and Doppler velocity V, i.e.: $V = c \cdot D$, where c is a calibration constant. We derived c by comparison with the velocity maps provided by the inversion of the IVM data: $c = 38 \pm 3$ km/s.

3.4. ERROR ANALYSIS

We performed a statistical analysis of the errors in the Stokes parameter measurements and derived the errors in the inferred magnetic fields. From analysis of the polarization images, we estimate the following rms noise in the polarization measurements: Stokes V/I : ± 0.0023, Stokes Q/I : ± 0.0018; Stokes U/I : ± 0.0018. For Stokes Q and U the rms noise values are slightly smaller because we applied a weighted running average to the Stokes images to increase the signal-to-noise ratio even though this averaging slightly reduced the spatial resolution for the linear polarization maps. The Stokes Q and U maps show signals almost a factor of two smaller than Stokes V, therefore the effective signal-to-noise ratio is still considerably larger than for the V maps.

From the errors in the Stokes measurements, we estimate the systematic calibration error in longitudinal field at 70 G with 60 G rms noise and a threshold of 55 G. For the transverse field the estimated systematic error is 85 G with 60 G rms noise and a threshold of 180 G. Here, the rms noise is defined as the error when measuring the same quantity multiple times. The threshold is the smallest value that can be measured above the background zero level noise.

The error in measuring the vector field direction is highly dependent upon the strength of the magnetic field. The stronger the field, the more accurate the direction estimate. From our calculations, it appears there is a maximum error at each field strength. But the average error is always between 0° and the maximum value. Table I shows the change in average and maximum errors for the zenith and azimuth angles as a function of field strength. In the table, $|\boldsymbol{B}|$ is the absolute value of the vector field and B_{trans} is the vector field component transverse to the LOS.

TABLE I
Error estimates in the direction of the magnetic field vectors

	Zenith Angle Errors			Azimuth Angle Errors	
$\|\boldsymbol{B}\|$	Avg [deg]	Max [deg]	B_{trans}	Avg [deg]	Max [deg]
250	10.0	20.0	200	12.2	25.0
500	5.0	12.0	400	5.0	8.0
1000	3.0	6.0	600	2.5	4.0
1250	2.2	4.0	800	1.8	2.5
1800	1.6	3.2			

From the statistical distribution of the field strengths, we estimate that the typical $|\boldsymbol{B}|$ observed was about 1000 G. Therefore, we can say that the typical average error in estimating the zenith angle is about 3°. The maximum error is about 6°. For the transverse components, the typical value was probably 400 G. Therefore, for the azimuth angle we have typically a 5° error in average and 8° maximum error.

These are just the statistical errors derived only from known measurement errors. It is extremely difficult to evaluate the errors in the vector direction that are related to the specific type of observation we made, i.e. measuring the polarization at a single wavelength position with a single and rather broad bandpass filter. We do not consider magneto-optical effects, but we do not expect that they are important as far out in the wing of the line as we were. In addition, we cannot evaluate the effects on the magnetic measurements due to Doppler shifts of the spectral line and other effects that may change the line profile. A comparison of the magnetic vector fields derived from FGE data and the corresponding IVM vector fields reveal that the zenith angle differences are mostly smaller than 5-10°. The differences in the azimuth angle estimates are usually bigger but they are also generally below 10°, with some areas (especially in penumbral regions) where the difference can rise up to about 20°.

We estimate the errors in the Doppler velocities of about ± 0.2 km/s with an rms noise of 0.11 km/s. We want to emphasize that the derived Doppler velocity maps probably underestimate the true line-of-sight velocities. Only measurements at multiple wavelengths across the spectral line can provide highly accurate velocity values.

4. Observations

4.1. FLUX EMERGENCE OVERVIEW

Active region NOAA 8844 had only two, small, stable sunspots until January 24. Rapid growth started late on the 24th or early on the 25th. The region continued growing for only about another 24 h after January 25. Our observations (Figure 1) began on the 25th at 15:50 UT and ended at 19:16 UT that day. At the time of the observations the active region was located at approximately 5°N 30°W.

Figure 1 shows NOAA 8844 at 17:57 UT as it appeared in the wing of the Ca I line (1.A), in a longitudinal magnetogram (1.B), in a Dopplergram (1.C), and in the blue wing of Hα (1.D). Note the thin dark fibrils in the center of the region, evident in the Ca I filtergram. These fibrils are characteristic of flux emergence in growing sunspot regions (Bray and Loughhead, 1964). The Dopplergrams show that the dark fibrils (each ≈ 3000 km long) were rising through the photosphere with typical velocities of at least 1 km/s. Flux emergence was episodic, with each dark fibril and its signature of upwelling in the Dopplergrams being visible for 5 to 10 minutes. The Hα images show signatures of an arch filament system, a characteristic feature of growing active regions (Bruzek, 1967). The tops of the arches are prominent in the Hα sequence, because they were rising, and while we cannot measure the exact rate of growth, the fact that they are clearly seen at 0.8 Å in the blue wing indicates an upward velocity of about 35 km/s. Also prominent in the Hα images are the Ellerman bombs (Ellerman, 1917; Kurokawa *et al.*, 1982; Nindos and Zirin, 1998), which have very broad, bright Hα wings and in our filtergram appear as brightenings roughly 1.5 arcsec in diameter. Georgoulis *et al.* (2002) analyze the Ellerman bombs in NOAA 8844 in detail.

There were three principal sites of flux emergence, as indicated by the large dashed ellipses in Figure 3. One (labeled with a 'C' in Figure 3.1) was in a supergranule adjacent to the follower spot and the two others were in supergranules just east of the center of the active region. Although we use the word, 'supergranules,' we note that they were only about 10 000 km in diameter instead of the more usual 30 000 km. However, the velocities – upwelling at the center and downflow along the edges – are characteristic of supergranules. The horizontal velocity pattern, with 0.3 – 0.5 km/s flows from the center, is also typical of supergranules. The vertical velocity pattern was determined from the

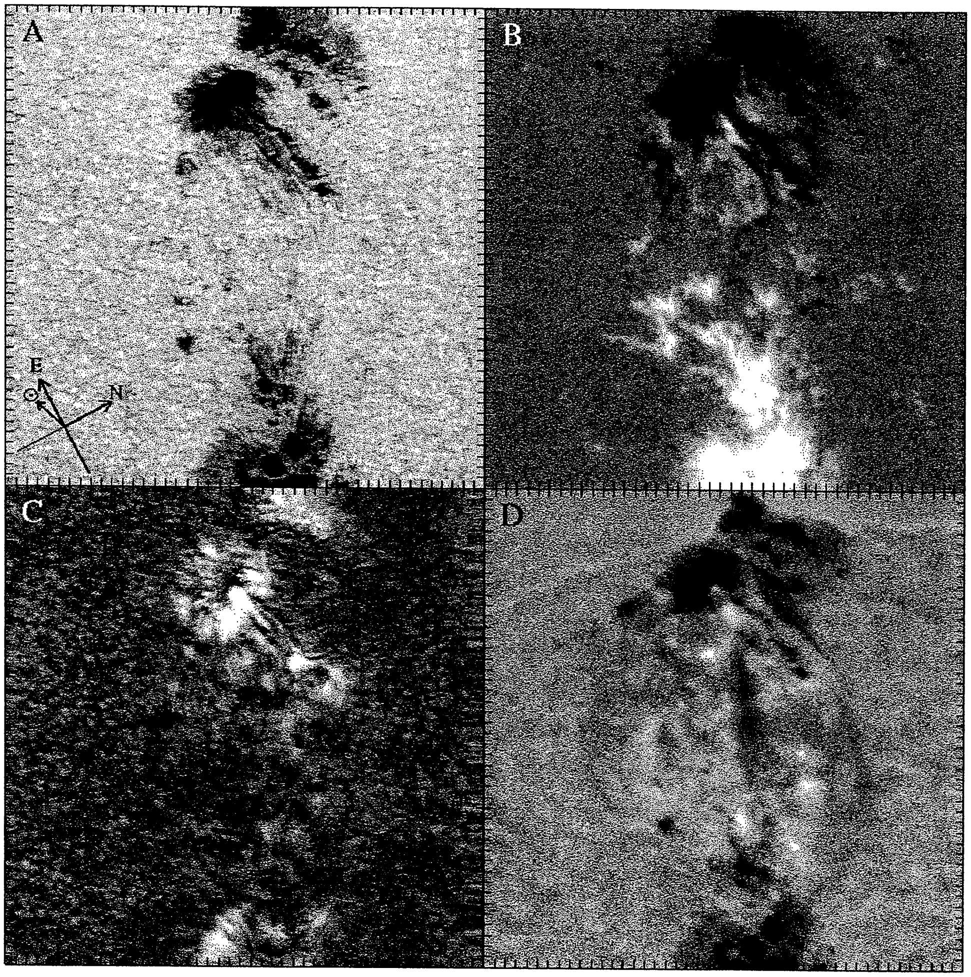

Fig. 1. Four views of NOAA 8844 recorded by FGE at approximately 17:57 UT on January 25, 2000. (A) Filtergram in the blue wing of the Ca I 6122 Å line. (B) Map of the line-of-sight longitudinal magnetogram. (C) Dopplergram; bright corresponds to a blue shift, i.e. a flow motion towards the observer. (D) Filtergram at 6562 Å: Hα – 0.8 Å. The images have a field of view of 90×90 arcsec and the tick mark separation is 2". The orientation of the AR and the Sun center direction are shown in the lower left corner of image A.

Dopplergrams. Cross-correlations of the pattern of granulation visible in successive Ca I line wing images determined the horizontal velocity pattern (Shine, 2001). A check of magnetic element motions vs. the

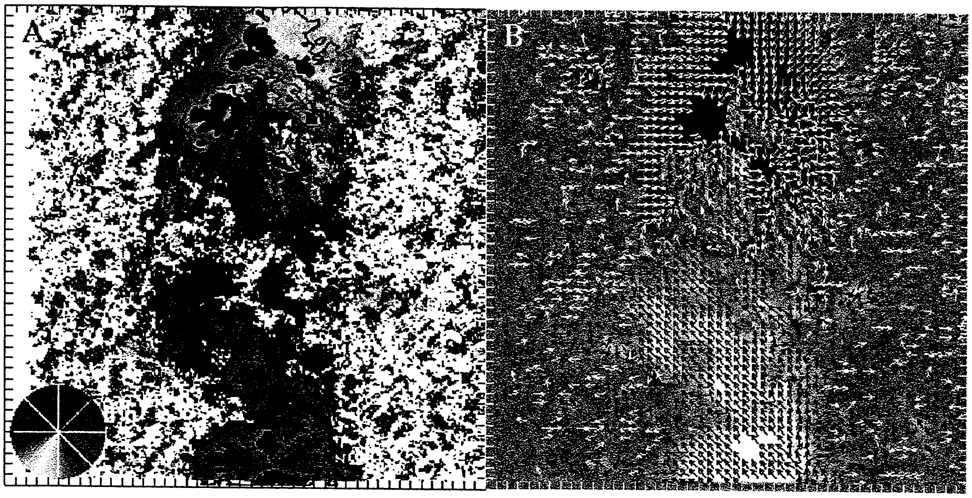

Fig. 2. (A) Color-coded map showing the orientation (azimuth) of the transverse magnetic field component. The color wheel in the lower left corner explains the vector direction (imagine the vector pointing from the center of the wheel towards the rim. The black areas indicate the location of the spot umbrae and the contours outline the penumbrae. The white areas do not show any data. (B) Same as A but with the field vector orientation expressed by arrows plotted over the corresponding longitudinal magnetogram. Tick mark separation is 2".

granulation horizontal velocities showed general agreement, so the surface motions appear to have been largely determined by the convective flows of the supergranulation.

To a first approximation, we can say that the magnetic fields emerged in a wide band of horizontal flux ropes between the two major spots. Figure 2, which shows the vector field orientations, reveals that the direction of the transverse field in the flux emergence region was remarkably uniform, as shown by the purple and red area in the figure. Purple corresponds to fields tilted $\approx 20°$ counterclockwise from the line connecting the leader and follower spots and red corresponds to $\approx 60°$ tilt. The strength of the transverse component in the flux emergence region did not vary greatly.

In general, negative poles flowed toward, and merged with, the follower spot, and positive poles flowed toward, and merged with, the leader spot. Typical velocity of the flow was 0.3 km/s. This emerging flux region was similar to the one studied recently by Strous *et al.* (1996)

and Strous and Zwaan (1999) and to the three regions studied by Lites, Skumanich, and Martinez Pillet (1998). However, the high resolution of our observations and the unvarying image quality from frame to frame revealed an important new fact: many of the emergent magnetic features, as seen in the longitudinal magnetograms, appeared to be dipolar.

4.2. MAGNETIC PROPERTIES OF MOVING DIPOLAR FEATURES

Over an interval of 206 min, we observed approximately 20 MDFs in an area of about 5×10^8 km^2. They were pairs of magnetic poles, each with an area of about 5×10^5 km^2, that moved together as obviously joined features. Most of the MDFs first appeared near the center of one of the three supergranules located west of the negative polarity, trailing sunspot (see Figure 3.1). Most migrated at a nearly constant velocity between 0.3 and 0.8 km/s from the supergranule centers toward the edges and/or into the sunspot. However, for short periods an MDF could dash at almost 1 km/s. We interpret the sudden accelerations and decelerations as interactions with the surrounding flow fields. This idea is supported by the observation that frequently, during the changes in speed, the MDFs also changed shape, mainly stretching or shrinking.

In the supergranule cell nearest the follower spot (ellipse labeled ‘C’ in Figure 3.1), only a few MDFs were moving westward, i.e. toward the edge of the cell opposite to the spot; the majority moved towards the spot and eventually merged with it. In all cases the polarity of the part closest to the spot was opposite to the polarity of the spot itself. This is opposite to the orientation in most of the dipolar MMFs observed in decaying sunspots (Harvey and Harvey, 1973).

Figure 3 shows a time series of longitudinal magnetograms that follows the position and evolution of two MDFs (ellipses labeled ‘a’ and ‘b’) as they approached the negative-polarity trailing spot. In the figure it is possible to see several more MDFs than the two we highlighted.

MDF ‘b’ approached the spot and merged with it. Once the MDF drew close to the spot, the positive feature nearest the spot elongated slightly then gradually disappeared (Figures 3.2 and 3.3). Conversely, when the negative part approached the spot, part of the spot itself appeared to extend towards it, to merge with it, and then to retract again (Figures 3.4 and 3.5). When an MDF approached the west edge of the supergranule (pointed out by the white arrow in Figure 3.2) from the east, its negative part disappeared and its positive part remained. Similarly, MDFs approaching from the opposite side left only a trace of their negative

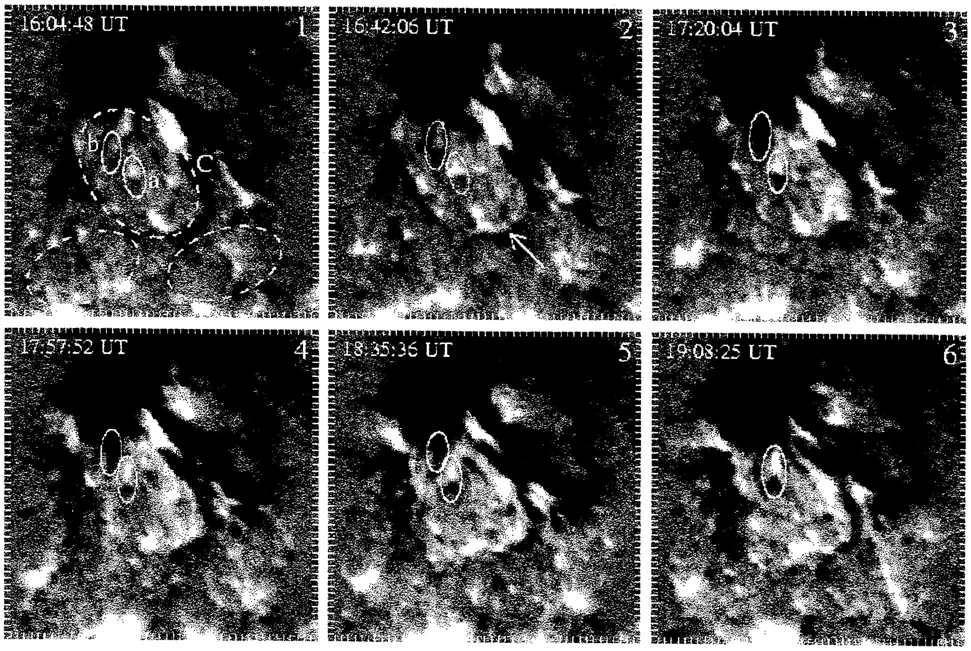

Fig. 3. Sequence of longitudinal magnetograms showing MDFs near the following (negative) spot of NOAA 8844 (black area at top). Most MDFs appeared in the supergranules outlined by the large dashed ellipses (frame 1). The small ellipses, marked by 'a' and 'b' in frame 1, follow the evolution of two such MDFs while they migrate towards the spot. The dashed ellipse labeled with C in frame 1 is the supergranule cell discussed in the text. The arrow in frame 2 indicates the location of the western boundary of the supergranule C.

fields. The movie[1] of the magnetic evolution at the supergranule cell boundary gives the impression that positive and negative fields were canceling, which could mean they were reconnecting and/or submerging.

The lifetimes of MDFs varied from tens of minutes to hours. For example MDF 'a' in Figure 3 is the most persistent one in our recordings. It survived for almost the entire 3.5 h of the sequence. In the last frame (Figure 3.6) its positive polarity appeared to extend towards the negative spot and it was probably about to be swallowed by the sunspot. Most MDFs disappeared only when they reached the edge of a supergranule or a sunspot, but a few faded and disappeared before reaching such a boundary. Figure 4 shows five typical MDFs. Three of them (labeled 1,

---

[1] See web page: sd-www.jhuapl.edu/FlareGenesis/Science/results.html#Movies

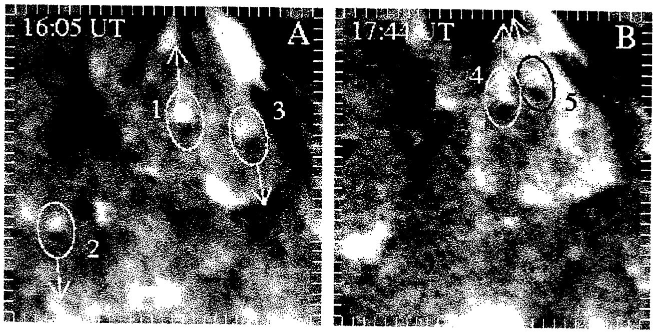

Fig. 4. Longitudinal magnetograms with ellipses indicating the location of the five MDFs discussed in the text. The arrows show the direction of motion of the MDFs. The tick mark separation is 1".

4, and 5) moved toward the follower spot, located on the upper edge of the images, and two moved away from it (2 and 3).

Figure 5 shows the vector fields in the five MDFs. In each MDF, the vectors point to the left in the positive and negative parts, revealing that each MDF vector magnetic field is a shallow U-loop. Also in each MDF the vectors in the negative part are steeper than the vectors in the positive part.

For each MDF we derived the dimensions and field characteristics along a line that goes through the center of its two magnetic parts. Along this line we calculated the average for four parameters over a width of seven pixels ($\approx 1.2'' \approx 1000$ km). The four parameters are the absolute field strength $|\boldsymbol{B}|$, the field strength component parallel to the local vertical $B_{//\ \mathrm{local}}$, the local zenith angle γ_{local}, and the line-of-sight velocity. Their variation along the MDF length is shown in Figure 6. Each line type represents a different MDF. We aligned the traces so that the neutral lines at the centers of the MDFs coincide. The plot shows that all the MDFs had similar characteristics. Each MDF attained a maximum of the longitudinal field strength at around 200 G, and each reached the peak approximately 1" from the neutral line that bisected the respective MDF (Figure 6.B). In contrast, γ_{local} showed a clear asymmetry with respect to the neutral line (Figure 6.C). The field lines in the negative part of each MDF were more perpendicular to the local surface than the ones in the positive part. The field angle peaked on average at 50° in the negative part, while its peak in the positive part was only 20°.

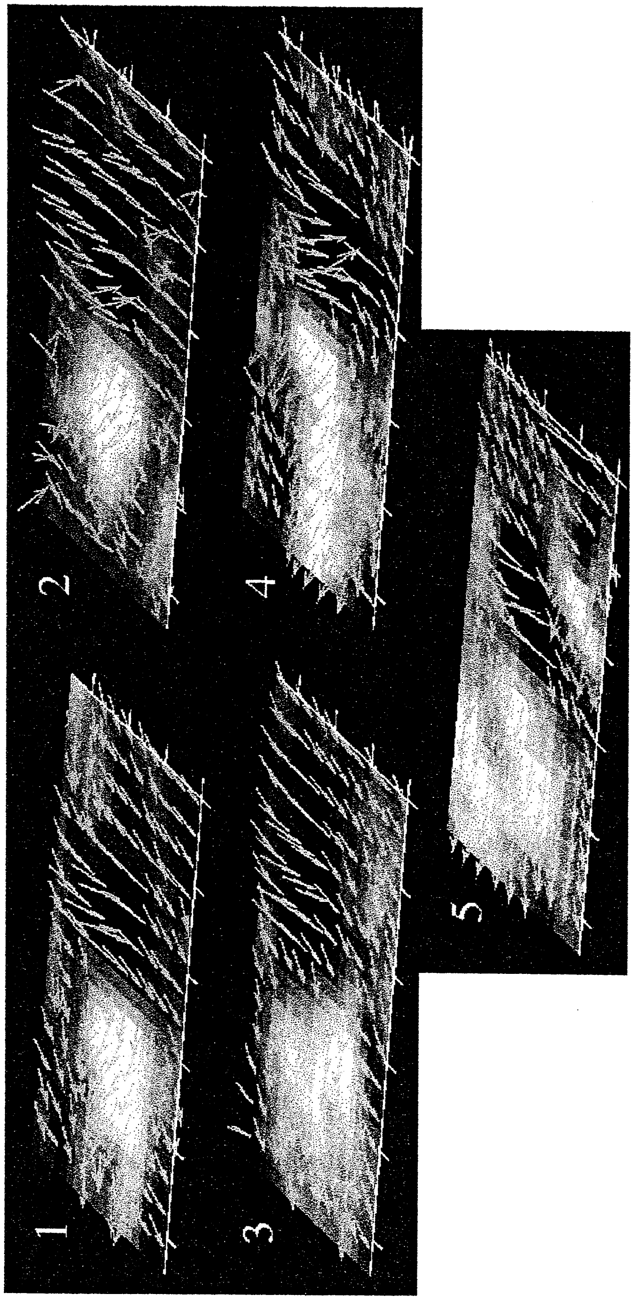

Fig. 5. View in perspective of the magnetic vector field geometry for the 5 MDFs of Figure 4. In each case, the vectors (yellow arrows) point downward and to the left in the negative part and upward and to the left in the positive part.

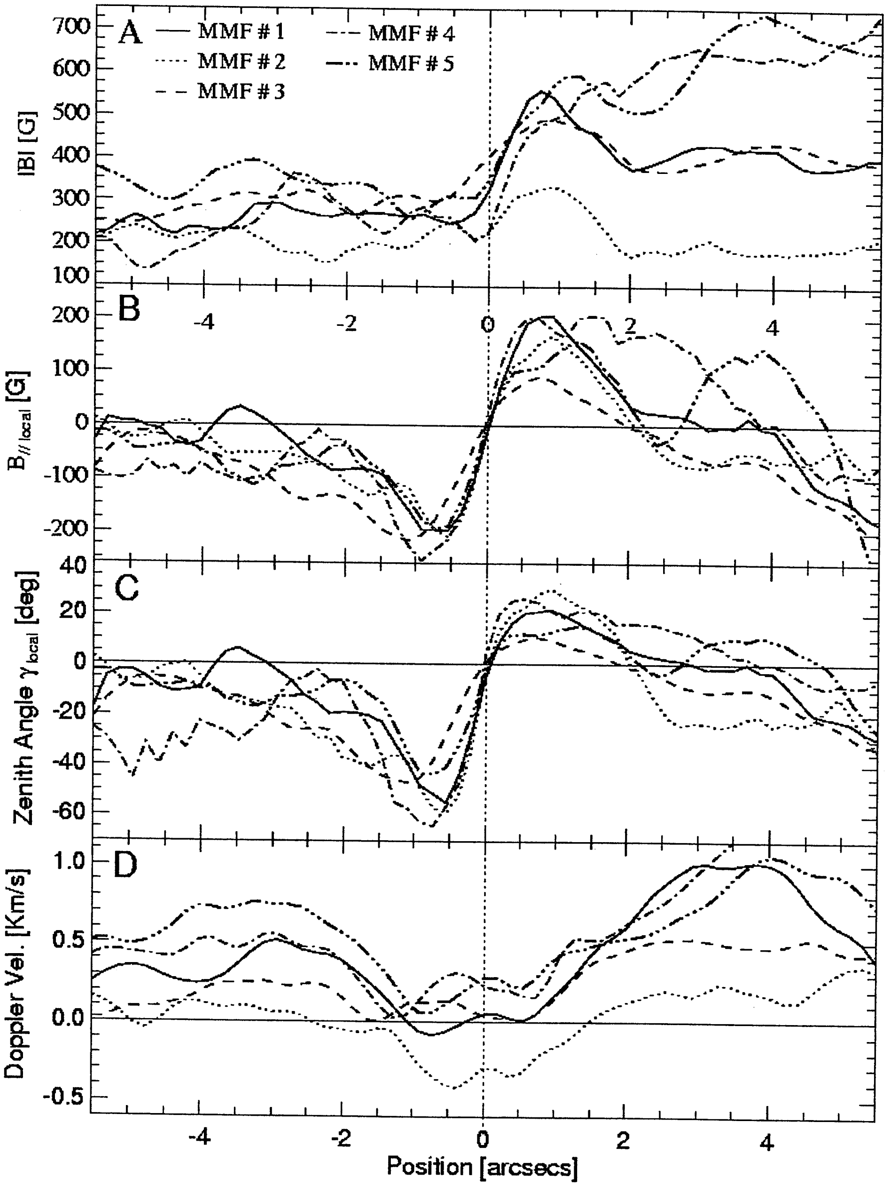

Fig. 6. Properties of the five MDFs highlighted in Figures 4 and 5. (A) Absolute value of the vector magnetic field strength. (B) Field strength of the vector component parallel to the local vertical (longitudinal field strength in the local coordinate frame). (C) Field inclination (zenith angle) in the local reference system: –90° is vertical down, 0° is horizontal, 90° is vertical up. (D) Plasma velocity parallel to the line-of-sight direction. Positive is towards the observer (upflow).

In general, the absolute field strength appeared to be greater in the positive parts than in the negative parts (see Figure 6.A). Moreover, the increase in |***B***| included even the fields just outside of each positive part. We believe that this is mainly due to the proximity of the positive parts of the MDFs to the sunspot and its stronger fields. This effect was more prominent in MDFs 4 and 5, since they were closest to the spot (compare their positions in Figure 4). On the other hand, MDF number 2, which was located very far from the spot, showed a quite flat field strength of about 220 G over its entire length. By just looking at |**B**| maps it is very difficult to identify the MDFs. This means that generally the magnetic field strength within the MDFs was not remarkably different from the field strength in the adjacent areas. What made the MDFs visible in the longitudinal field maps was their vector field inclination. In the surrounding areas, the field lines were nearly horizontal, on average –5° (i.e. slightly negative polarity), while the field line inclination within the MDFs reached relatively high angles with respect to the surface. We therefore believe that the MDFs are not single isolated dipoles emerging from below the surface, but most likely dips in the canopy of horizontal field lines that filled the entire area of emerging flux.

4.3. MATERIAL FLOW IN MDFS

An important feature of the MDFs is their Doppler signature, which is shown in Figure 6.D. All five of the MDFs there had a net downflow with respect to the surroundings. In particular, the Doppler curves show two clear dips coincident with the location of maximum longitudinal field strength and also the highest field angle with respect to the surface. This could be evidence for drainage along the field lines of the dense plasma that was carried into the upper photosphere / lower chromosphere during flux emergence. Note that the downflow was not confined to the parts of the MDFs with the strongest longitudinal field. Each whole MDF was sinking, according to the Dopplergrams.

We have already remarked on how the MDFs interacted with the negative sunspot, namely, the positive parts disappeared and the negative parts merged with the negative fields of the spot penumbra. After each merger, we could not distinguish the MDFs in the magnetograms, but in the Dopplergrams the downflow signature persisted, and one can follow the MDFs as they pushed into the penumbra even though the penumbra had a strong outward Evershed flow. We are reminded of Parker's article (Parker, 1978) predicting that draining the material of magnetic flux ropes

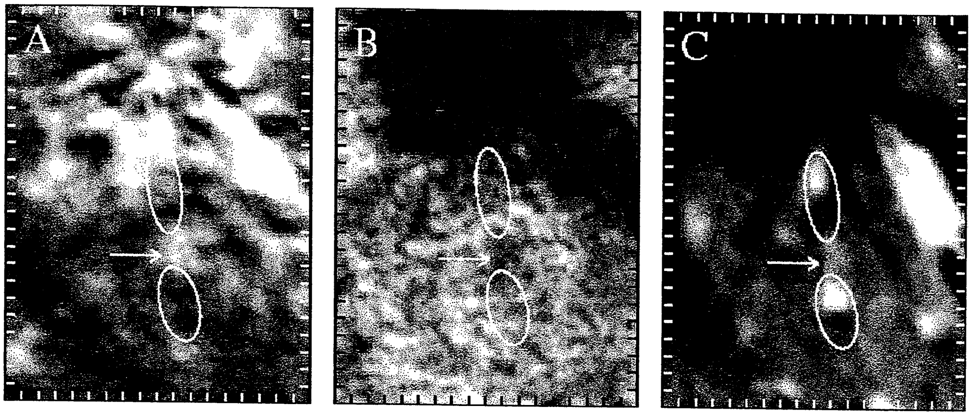

Fig. 7. Enlarged images of the Dopplergram (A), contrast enhanced Ca I line wing filtergram (B), and LOS longitudinal magnetogram (C) of the western edge of the trailing sunspot recorded at 16:07 UT. The ellipses indicate the location of two MDFs moving towards the spot. They are linked by a dark, rising fibril whose location is pointed out by the arrow. The fibril is a dark thread in the filtergram (B) and is associated with an upflow visible in the Dopplergram (A). Figure 8 sketches the field lines that could produce this particular configuration.

will initiate enhancement of sunspot field strength by convective collapse. We have not yet examined our data for magnetic field enhancements precisely associated with MDF arrival at the penumbra's edge, but we did note that the photosphere near the spot darkened as the MDFs arrived. Our results are consistent with Lites, Skumanich, and Martinez Pillet (1998) who found downflows on edges of sunspots in an emerging flux region.

Figure 7 illustrates the relationships linking the dark threads of emerging flux, the upward flows, and the MDFs. In the figure we can see two MDFs that appear to be connected by a dark thread in the photospheric image (indicated by the arrow in Figure 7.B), co-located with a white thread in the Dopplergram (Figure 7.A) indicating an upflow. The MDF near the center of Figure 7.C is about to merge with the spot, and its positive part is stretching. Note in Figure 7.A the two dark patches (downflows) that are exactly co-located with the two more vertical magnetic parts of the lower MDF. The figure shows what we found to be the general case: MDFs with their entrained downflows appeared at the far ends of the dark threads in the continuum pictures.

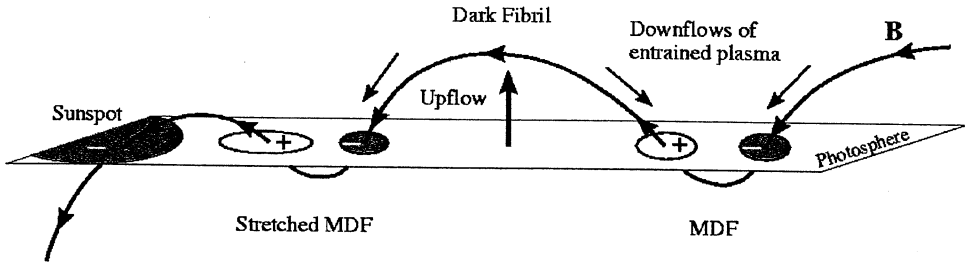

Fig. 8. Sketch summarizing the relationship between emerging dark fibrils and the MDFs seen in longitudinal magnetograms. The curve ***B*** indicates the magnetic flux rope.

5. Summary and Conclusions

A summary of our findings: moving dipolar features have been discovered in emerging magnetic flux. They move horizontally toward sunspots and supergranule boundaries. All the MDF pairs, wherever they occurred in the emerging flux region, were oriented opposite to the main active region polarities, i.e., each positive (leading polarity) part was eastward, not westward, of its corresponding negative (following polarity) part. The MDFs were remarkably similar in size, field strength, and orientation. Downflows were persistent at each pole. The MDFs were born and are sustained in regions with nearly horizontal fields (average elevation ≈ 5°). They expired, apparently with a downward plunge, at the edges of sunspots and supergranules. Vector magnetograms (Figure 5) show that the MDFs are really magnetic U-loops stitched into the upper photosphere, where the Ca I line is formed.

Figure 8 summarizes our interpretation of the data. We emphasize that the principal component of magnetic field in MDFs is the horizontal field. The observations show that bulges in nearly horizontal flux ropes at the upper photosphere create dark threads in the white-light images. The rising segments of flux rope are about 3000 km long. At a distance of another 3000 km, we find connected MDFs, whose poles are approximately 1000 km apart. Plasma in the dark threads would rise, cool (as indicated by the darkening), become more dense, and then slide downward into the MDFs. The fact that all the MDFs were similar in size and field orientation suggests that they result from a hydrodynamic instability with a characteristic wavelength of approximately 1000 – 3000 km.

Perhaps the Kelvin-Helmholtz instability (KHI) (Min, 1997; Ryu, Jones, and Frank, 2000) is involved. See for example, Diver, Brown, and Rust (1996) who proposed that the KHI evolves into centers for the tearing mode instability, which would account for the Ellerman bombs that frequently appeared above the MDFs.

It is interesting to contrast the properties of the inflowing MDFs with the dipolar outflowing MMFs previously reported around decaying sunspots. Outflowing MMFs move faster than the surrounding granules; they may appear at first to be a continuation of penumbral fibrils or they may develop anywhere in the moat; the two poles separate gradually; and they disappear when they reach the sunspot moat, or they just fade away (Shine and Title, 2001). The pole nearest the spot usually has the same polarity as the spot (Harvey and Harvey, 1973). However, Yurchyshyn, Wang, and Goode (2001) observed some outflowing dipolar MMFs with the nearest pole polarity opposite to that of the parent spot. This is the same orientation that we found for the inflowing MDFs. The inflowing MDFs that we observed moved with the surrounding material; they were associated with the dark fibrils of the emerging flux; they could develop anywhere in the emerging flux region. When an MDF reached the negative-polarity sunspot, the positive part dissolved and the spot developed a peninsula of negative field that stretched out to incorporate the negative part, which trailed the positive one.

Ryutova *et al.* (1998) and Harvey and Harvey (1973) suggested that outflowing dipolar MMFs are convex kinks in the horizontal fields extending outside penumbrae. From their shape, they are called Ω-loops. The sunspot-decay MMFs in our own observations would appear to fit this description. Near the northern edge of the trailing spot we saw one MMF flowing outwards, and indeed, its vector field configuration revealed an Ω-loop. However, there seems no escaping the conclusion that the sunspot-building MDFs are U-loops formed between segments of emerged flux. The MDFs cannot be kinks in the rising flux ropes because then we would see the parts with opposite polarity separating. Instead, the two MDF parts formed by pulling apart, but then they remained connected for the entire life span of the MDF. We conclude that they formed when plasma on just emerged field lines cooled, then pooled, then distorted the field lines, making a concave depression in them. The distorted segment, a U-loop, is swept by the convective flows to the edge of a sunspot or supergranule. There the entrained material can slide down one of the main legs of the flux rope bundle in the active region, which presumably extends deeply into the convection zone, possibly all the way to the base.

These observations illustrate how knots of plasma entrained in segments of emerging flux ropes are propelled along the solar surface, like pearls on a string, towards sunspots and the chutes at supergranules boundaries. There, they can slide back down into the sea of plasma from which they came. The observations also illustrate dramatically how vector magnetograms facilitate the interpretation of active region phenomena.

Our results may have an application that is wider than active regions – there is a background pattern of dipolar fields everywhere on the sun. Dipolar features are often born with the same pattern as those seen here, namely, the positive and negative poles are born together, then separate to assume a characteristic distance from each other. Since our vector magnetic field observations showed that the horizontal field in the MDFs is far more important than the vertical component, we suggest that there could be a background pattern of horizontal fields everywhere. They could reside in the convectively stable layer just above the granulation. The plasma sloshing around in those fields should often form pools and deform those fields, giving the appearance in longitudinal magnetograms of magnetic dipoles coming and going. The difficult-to-understand background fields (Zhang *et al.*, 1998) may, in part, be due to dips in horizontal fields not observed, so far. Not until there are very sensitive vector field measurements of the weak fields outside active regions will we know the true structure of the ephemeral dipolar features.

Acknowledgments

We are grateful to Dick Shine for calculating the horizontal photospheric flows from the Ca I line wing filtergrams. We thank Harry Eaton for extracting the raw images from the flight tapes, and for his help in developing the algorithms used to co-align the images. We also thank Brigitte Schmieder for reading and commenting on the manuscript. This work was supported by NSF under grants OPP-9615073 and OPP-9909167, and by NASA grants NAG5-4955, NAG5-5139, and NAG5-8331 and by various AFOSR grants.

References

Bernasconi, P.N., Rust, D.M., Murphy, G.A., and Eaton, H.A.C.: 1999 in T.R. Rimmele, K.S. Balasubramaniam, and R.R. Radick (eds.), *High Resolution Solar Physics: Theory, Observations, and Techniques*, Astron. Soc. Pacific Conf. Ser. 183, Sunspot, NM, p. 279.

Bernasconi, P.N., Rust, D.M., Eaton, H.A.C., and Murphy, G.A.: 2000, in R.K. Melugin and H.-P. Roeser (eds.), *Airborne Telescope Systems*, Proc. SPIE 4014, Munich, p. 214.

Bernasconi, P.N., Rust, D.M., Murphy, G.A., and Eaton H.A.C.: 2001 in , M. Sigwarth (ed.), *Advanced Solar Polarimetry – Theory, Observation, and Instrumentation*, Astron. Soc. Pacific Conf. Ser. 236, Sunspot, NM, p. 399.

Bray, R.J. and Loughhead, R.E.: 1964, *Sunspots*, Chapman & Hall, London.

Brickhouse, N.S. and LaBonte, B.J.: 1988, *Solar Phys.* 115, p. 43.

Bruzek, A.: 1967, *Solar Phys.* 2, p. 451.

Diver, D.A., Brown, J.C., and Rust, D.M.: 1996, *Solar Phys.* 168, p. 105.

Ellerman, F.: 1917, *Astrophys. J.* 46, p. 298.

Gary, G.A. and Hagyard, M.J.: 1990, *Solar Phys.* 126, p. 21.

Georgoulis, M.K., Rust, D.M., and Bernasconi P.N.: 2002, *Astrophys. J.* (submitted).

Harvey, K.L. and Harvey, J.W.: 1973, *Solar Phys.* 28, p. 61.

Kurokawa, H., Kawaguchi, I., Funakoshi, Y., and Nakai, Y.: 1982, *Solar Phys.* 79, p. 77.

Lites, B.W., Skumanich, A., and Martinez Pillet, V.: 1998, *Astron. Astrophys.* 333, p. 1053.

Metcalf, T.R.: 1994, *Solar Phys.* 155, p. 235.

Mickey, D.L., Canfield, R.C., LaBonte, B.J., Leka, K.D., Waterson, M.F., and Weber, H.M.: 1996, *Solar Phys.* 168, p. 229.

Min, K.W.: 1997, *Astrophys. J.* 482, p. 733.

Nindos, A. and Zirin, H.: 1998, *Solar Phys.* 182, p. 381.

Nye, A.H., Thomas, J.H., and Cram, L.E.: 1984, *Astrophys. J.* 285, p. 381.

Parker, E.N.: 1978, *Astrophys. J.* 221, p. 368.

Parker, E.N.: 1994, *Astrophys. J.* 433, p. 867.

Ronan, R.S., Mickey, D.L., and Orrall, F.Q.: 1987, *Solar Phys.* 113, p. 353.

Rust, D.M.: 1994, *Opt. Eng.* 33, p. 3342.

Ryu, D., Jones, T.W., and Frank, A.: 2000, *Astrophys. J.* 545, p. 475.

Ryutova, M., Shine, R.A., Title, A.M., and Sakai, J.I.: 1998, *Astrophys. J.* 492, p. 402.

Schmieder, B., Bernasconi, P.N., LaBonte, B.J., and Rust, D.M.: 2002, (in preparation).

Sheeley, N.R., Jr.: 1969, *Solar Phys.* 9, p. 347.

Shine, R.A.: 2001, private communication.

Shine, R.A. and Title A.M.: 2001, in P. Murdin (ed.), *Encyclopedia of Astronomy and Astrophysics*, Inst. of Physics Pub., London, p. 3209.

Skumanich, A. and Semel, M.: 1996, *Solar Phys.* 164, p. 291.

Spruit, H.C., Title, A.M., and van Ballegooijen, A.A.: 1987, *Solar Phys.* 110, p. 115.

Strous, L.H., Scharmer, G.B., Tarbell, T.D., Title, A.M., and Zwaan, C.: 1996, *Astron. Astrophys.* 306, p. 947.

Strous, L.H. and Zwaan, C.: 1999, *Astrophys. J.* 527, p. 435.

Yurchyshyn, V.B., Wang, H., and Goode, P.R.: 2001, *Astrophys. J.* 550, p. 470.

Zhang, J., Lin, G., Wang, J., Wang, H., and Zirin, H.: 1998, *Astron. Astrophys.* 338, p. 322.

Statistics, Morphology, and Energetics of Ellerman Bombs

Manolis K. Georgoulis, David M. Rust and Pietro N. Bernasconi
The Johns Hopkins University Applied Physics Laboratory,
11100 Johns Hopkins Rd., Laurel MD, 20723, USA
and

Brigitte Schmieder
Observatoire de Paris, Section Meudon, 92195 Meudon Principal Cedex, France

ABSTRACT

We investigate the statistical properties of Ellerman bombs in the dynamic emerging flux region NOAA 8844, underneath an expanding arch filament system. High-resolution chromospheric $H\alpha$ filtergrams (spatial resolution $0.8''$), as well as photospheric vector magnetograms (spatial resolution $0.5''$), and Dopplergrams, have been acquired by the balloon-borne Flare Genesis Experiment. $H\alpha$ observations reveal the first "seeing-free" data set on Ellerman bombs and one of the largest samples of these events. We find that Ellerman bombs occur and recur in preferential locations in the low chromosphere, either above, or in the absence of, photospheric neutral magnetic lines. Ellerman bombs are associated with photospheric downflows and their loci follow the transverse mass flows on the photosphere. They are small-scale events, with typical size 1.8×1.1 $arcsec^2$, but this size depends on the instrumental resolution. A large number of Ellerman bombs are probably undetected, due to limited spatial resolution. Ellerman bombs occur in clusters which exhibit fractal properties. The fractal dimension, with an average value ~ 1.4, does not change significantly in the course of time. Typical parameters of Ellerman bombs are interrelated and obey power-law distribution functions, as in case of flaring and sub-flaring activity. We find that Ellerman bombs may occur on separatrix, or quasi-separatrix, layers, in the low chromosphere. A plausible triggering mechanism of Ellerman bombs is stochastic magnetic reconnection caused by the turbulent evolution of the low-lying magnetic fields and the continuous re-shaping of separatrix layers. The total energies of Ellerman bombs are estimated in the range $(10^{27}, 10^{28})$ erg, the temperature enhancement in the radiating volume is $\sim 2 \times 10^3$ K and the timescale of radiative cooling is short, of the order of a few seconds. The distribution function of the energies of Ellerman bombs exhibits a power-law shape with an index ~ -2.1. This suggests that Ellerman bombs may contribute significantly to the heating of the low chromosphere in emerging flux regions.

Subject headings: Sun: chromosphere—Sun: flares— Sun: magnetic fields—Sun: photosphere—Sun: UV radiation

1. Introduction

Ellerman (1917), in a pioneering work, reported a solar phenomenon "so extraordinary that it seemed hardly real". Spectroscopic studies at the Mount Wilson Solar Observatory had discovered a brilliant emission kernel at both wings of the $H\alpha$ line in several locations of the low chromosphere. These short-lived, small-scale events are now usually called Ellerman bombs (EBs).

The spectral profile of EBs consists of a deep absorption core at the $H\alpha$ line center with excess emission at the red and the blue wings of the line. The emission reaches a maximum at wavelengths $\sim H\alpha \pm 1$ Å and fades at typically $\sim \pm 5$ Å from the line center (Engvold & Maltby 1968; Severny 1968). An asymmetry with excess emission at the blue wing has been first reported by Koval & Severny (1970) and Bruzek (1972). Because of the peculiar appearance of bomb spectra on photographic negatives, EBs are also known as "moustaches". The first to confirm the identity between EBs and moustaches were McMath, Mohler, & Dodson (1960).

For decades, EBs have been known as frequent, short-lived brightenings, seen mostly at the wings of the $H\alpha$ line. They generally occur in areas of flux emergence and strong magnetic fields, such as the vicinity of the penumbra around isolated sunspots, and the interspot areas of new and dynamic emerging flux regions, beneath the expanding arch filament system (AFS). Zachariadis, Alissandrakis, & Banos (1987) estimated a mean occurrence rate of about 1.5 EBs min^{-1} in an area of size 18×24 $arcsec^2$. The typical sizes of EBs are of the order one *arcsec*. Mean lengths of 1 - 1.4 *arcsec* have been reported. In most cases, EBs appear as elongated structures with length typically 37 - 45% larger than their width (Kurokawa et al. 1982; Nindos & Zirin 1998). The typical EB lifetimes were estimated from early works to be ~ 20 *min* (Severny 1965). Bruzek (1972) and Vorpahl and Pope (1972), however, reported that certain EBs could be visible for times exceeding 1 *hr*. The estimation of EB durations depends critically on the temporal resolution (cadence) of the observing instrument, since EBs often tend to recur at approximately the same locations (Vorpahl & Pope 1972; Bruzek 1972; Zachariadis, Alissandrakis, & Banos 1987). The generally accepted mean lifetime of EBs is 10 - 14 *min* (Roy & Leparskas 1973; Kurokawa et al. 1982; Payne 1993; Nindos & Zirin 1998). In a recent, high-cadence (~ 1 *s*) series of observations, Qiu et al. (2000) reported mean EB lifetimes of 10 - 20 *min*.

In studies of the surroundings of EBs, Severny (1968) detected intense ascending chromospheric motions and Rust (1968) found that EBs occur above "satellite" (opposite polarity) sunspots seen at the vicinity of well-defined spots. EBs are also associated with $H\alpha$ surges, whose threads ($\sim 5 \times 10^3$ km) follow the magnetic field lines calculated from current-free extrapolations (Rust 1968). Several EBs were found at the boundaries of well-defined magnetic structures (Roy and Leparskas 1973; Dara et al. 1997), related to dipolar emerging flux (Zachariadis, Alissandrakis, & Banos 1987), and moving magnetic features (Nindos and Zirin 1998).

Despite the fact that EBs have long been known, their triggering mechanism remains puzzling. In early studies by Severny and co-workers (for a review see Severny 1964), EBs, or moustaches, were viewed as low-altitude sub-flares. This is still a highly debated viewpoint, with several issues yet to be resolved. One of these issues is the temporal profiles of EBs. In contrast to flares and sub-flares, the temporal profiles of EBs are rather symmetric (Payne 1993; Qiu et al. 2000). Flares and sub-flares, on the other hand, mostly show an impulsive, short rise phase, followed by a much longer, gradual decay phase. Other EB properties include association with facular granules (Bruzek 1972; Dara et al. 1987), $H\alpha$ filigree, calcium bright points and white-light faculae (Wilson 1981), facular points (Kitai & Muller 1984), photospheric filigree (Denker 1997), and moving magnetic features (Nindos and Zirin 1998). Vorpahl & Pope (1972), found that EBs correlate with photospheric bright points (BPs) at 3840 Å, which reach maxima at $\sim 3.5 \pm 1.0$ *min* prior to EB occurrence. Qiu et al. (2000) showed that EBs can also be seen as BPs in the Ultraviolet (UV) continuum emission at 1600 Å. These events occur in the temperature-minimum (T_{min}) region, at a height difference ~ 100 km from $H\alpha$ EBs.

Several models have been proposed to accommodate both the morphology of EBs and their spectral features. None of these models is generally accepted. Severny (1968) proposed a model with an expanding opaque layer that exhibits a velocity gradient with height, in a turbulent medium characterized by an ambient macro-turbulent velocity. A suitable choice of parameters could account for the distribution of intensity wings in moustaches, the blue asymmetry and the absorption gap at the $H\alpha$ line center. Pikel'ner (1974) argued that if EBs are triggered by magnetic reconnection, then the temperature should locally reach coronal values after field-line annihilation. Kitai (1983) found that a hot ($\Delta T \simeq 1.5 \times 10^3$ K) and dense ($\frac{\rho}{\rho_0} \sim 5$) gradient in the atmosphere may account for the line broadening in EBs. Kitai & Muller (1984) viewed EBs as events occurring in funnel-like, individual flux tubes, rather than as results of magnetic reconnection. Stellmacher & Wiehr (1991) attributed the moustache effect to the superposition of a hot component representing the magnetic structure, surrounded by a cool intergranular region. Hu, Song, & Li (1995) constructed the first magnetohydrodynamic (MHD) model of EBs. The model was based on magnetic reconnection on a current sheet, formed by the motion of an ascending plasmoid triggered by ponderomotive force. The local temperature in EBs reached 10^4 K. Higher temperatures were avoided, since the field-line annihilation products were carried away instantly by suprathermal particles. A similar MHD model, modified for a plasma with low ionization degree, was proposed by Ji, Song, & Li (2001). Ding, Hénoux, & Fang (1998) and Hénoux, Fang, & Ding (1998) proposed a non-thermal EB model that attributed the moustache line profiles to the bombardment of the low chromosphere by energetic particles. These particles were expected to originate from reconnection sites higher in the atmosphere. Diver, Brown, & Rust (1996) attributed EBs to a tearing-mode instability which was initially triggered by a purely hydrodynamical Kelvin-Helmholtz instability. The dissipated Ohmic power was estimated at $\sim 10^{21} erg\ s^{-1}$. Other energy estimates of EBs are in the range $(10^{25}, 10^{27})$ erg (Bruzek 1972; Hu, Song, & Li 1995; Hénoux, Fang, & Ding 1998).

To address the outstanding problem of the triggering cause of EBs, we performed a detailed analysis of EB emergence, morphology, statistical properties, and energetics. We used the first "seeing-free" sample of EBs, obtained by the balloon-borne Flare Genesis Experiment (FGE - Rust 1994a; Bernasconi et al. 2000; Bernasconi, Rust, & Eaton 2001). Several hundreds of EBs appear in our data, therefore making our sample adequate for statistical treatment.

The paper proceeds as follows: In § 2 we discuss the acquisition of the FGE data and the data reduction process. In § 3 we estimate the mean occurrence rate of EBs and describe their spatial distribution. In § 4 we discuss the morphology of EBs and their relation to the underlying photospheric conditions and to activity in the T_{min} region. In § 5 we perform the first statistical study of EBs, based on the fractal properties of the EB clustering process and on typical EB parameters, such as the spatial extent, peak and total activity. In § 6 we estimate EB energies relying on estimations of radiative losses and mass motions in EBs. In § 7 we propose an interpretation of EBs, supported by our observations. In § 8 we summarize our findings and discuss the implications of our results.

2. Flare Genesis Experiment and Active Region NOAA 8844

The data used in this work were collected during the second FGE flight, in January 2000. The flight duration was 17 days (January 10 to January 27). The apparatus was installed on a balloon-borne gondola and it circumnavigated the Antarctic continent at an altitude of 37 km, obtaining an un-obstructed, $24-h$ view of the solar disk[1]. The principal optic of the FGE was an 80 cm Cassegrain telescope (the largest solar telescope ever flown) with a $F/1.5$ light-weight, ultra-low expansion primary mirror, a single-crystal silicon secondary and a graphite-epoxy telescope tube. The tube structure provided high thermal stability and the silicon secondary mirror gave optimum heat transfer with minimum thermal distortion. For this reason, we believe that the acquired images are free from distortion due to turbulence in the telescope, or in the atmosphere (Bernasconi et al. 2000; Bernasconi, Rust, & Eaton 2001). The focal plane instrumentation consisted of a polarization analyzer unit (two liquid-crystal polarization modulators and a linear polarizing filter), a selection of 1.25 Å order-isolation filters, a 0.16 Å tunable Fabry-Pérot etalon filter (Rust 1994b) and refractive optics to record a $160-arcsec$ $\oslash$ section of the Sun on a 1024×1024-pixel CCD camera. The field of view of the CCD was 92×92 $arcsec^2$, the plate scale was 0.091 $arcsec$ per pixel, and the achieved image quality (spatial resolution) varied between 0.5 $arcsec$ and 0.8 $arcsec$, depending on the observed wavelength. To achieve a better signal-to-noise ratio, the images were interpolated into a uniform grid of 512×512 pixels, with pixel size equal to 0.18 $arcsec$.

FGE collected nearly simultaneous observations of the photospheric magnetic field vector, the line-

---

[1] For a complete description of the FGE mission see Bernasconi et al. (2000), as well as the FGE web site http://sd-www.jhuapl.edu/FlareGenesis/

of-sight (LOS) longitudinal photospheric velocity (from Dopplergrams) and filtergrams at the blue wing of the $H\alpha$ line. Let us discuss briefly each of these data sub-sets:

(1) The Stokes parameters required for vector magnetograms were obtained from observations at the red and the blue wings of the photospheric Ca I line (6122.2 Å). They were obtained from sequentially recorded sets of 12 filtergrams at the polarization states $I+Q$, $I-Q$, $I+U$, $I-U$, $I+V$ and $I-V$ at ±0.08 Å at the wings of the Ca I line. The Stokes images (Q/I), (U/I) and (V/I) were calculated from the normalized difference between measurements of opposite polarization states. The magnitudes of the LOS longitudinal and transverse magnetic field components were calculated following the method of Ronan, Mickey, & Orrall (1987). The precise location of the AR on the solar disk was found by comparison to simultaneous, full-disk Kitt Peak magnetograms. This enabled the calculation of the local reference system (LRS) photospheric magnetic field components. The resolution of the 180^o-ambiguity was qualitative, relying on a combination of a potential field solution and an empirical, expected orientation of the transverse component (Bernasconi et al. 2002).

(2) Dopplergrams were obtained by calculating the normalized difference between filtergrams obtained at the wings of the Ca I line. During each 12−image set, an averaging process was performed. Standard filters were applied to remove some effects of the 5 min oscillation and to cancel out image-to-image intensity variations introduced by vector polarimetric measurements.

(3) Filtergrams at the blue wing of the $H\alpha$ line (6562.8 Å) were obtained between each set of Stokes images. Corrections for the dark current and the gain function were applied and the filtergrams were carefully co-aligned by means of standard cross-correlation techniques. During the co-alignment process, the center of the AR was kept fixed at the center of the field of view.

Restrictions imposed by the observing plan, the instrument, the CCD detector, and the data storage medium resulted in a cadence varying in the range $(3.5, 7.5)$ min. The $H\alpha$ data refer solely to the blue wing of the line, at about 0.8 Å from the line center. For these reasons, we will not attempt any conclusions regarding either the temporal or the spectral profiles of EBs.

On January 25, 2000, FGE was observing the young, dynamic, emerging flux region NOAA 8844, just after the active region (AR) showed signs of rapid development. An expanding AFS was observed in $H\alpha$ and a multitude of EBs was detected beneath the large-scale structure. An uninterrupted data set was obtained for ~ 3.5 h (UT 15:50 - 19:16). The AR entered its declining phase 24 h after the observations. The AR's mean heliographic coordinates were 5^o N 30^o W. The axis of the AR formed a tilt angle of $\sim 28^o$ with the equator. The AR consisted of a compact pair of small sunspots which were moving apart rapidly. Although the AR produced no flares, some subflaring activity was reported by the NOAA Space Environment Center, with the most prominent sub-flares observed at 16:02, 16:27, 17:04 and 18:54 UT.

In this work, we will use the following FGE data:

(i) 55 vector magnetograms with a spatial resolution $\sim$ 0.5 $arcsec$ and a cadence ~ 3.5 min.

(ii) 28 Dopplergrams with a spatial resolution ~ 0.8 $arcsec$ and a cadence ~ 7.5 min.

(iii) 28 $H\alpha - 0.8$ Å filtergrams with a spatial resolution ~ 0.8 $arcsec$ and a cadence ~ 7.5 min.

The FGE data on AR NOAA 8844 were complemented by simultaneous observations by *Yohkoh*/SXT, SOHO/MDI, TRACE and the Imaging Vector Magnetograph (IVM) of the University of Hawaii. We have not yet fully retrieved this multi-instrument data collection. In this study, however, we make a first step in coupling the FGE data with a data set from TRACE which refers to UV 1600 Å continuum emission in the T_{min} region. We have selected 13 TRACE frames that are simultaneous with respective FGE frames.

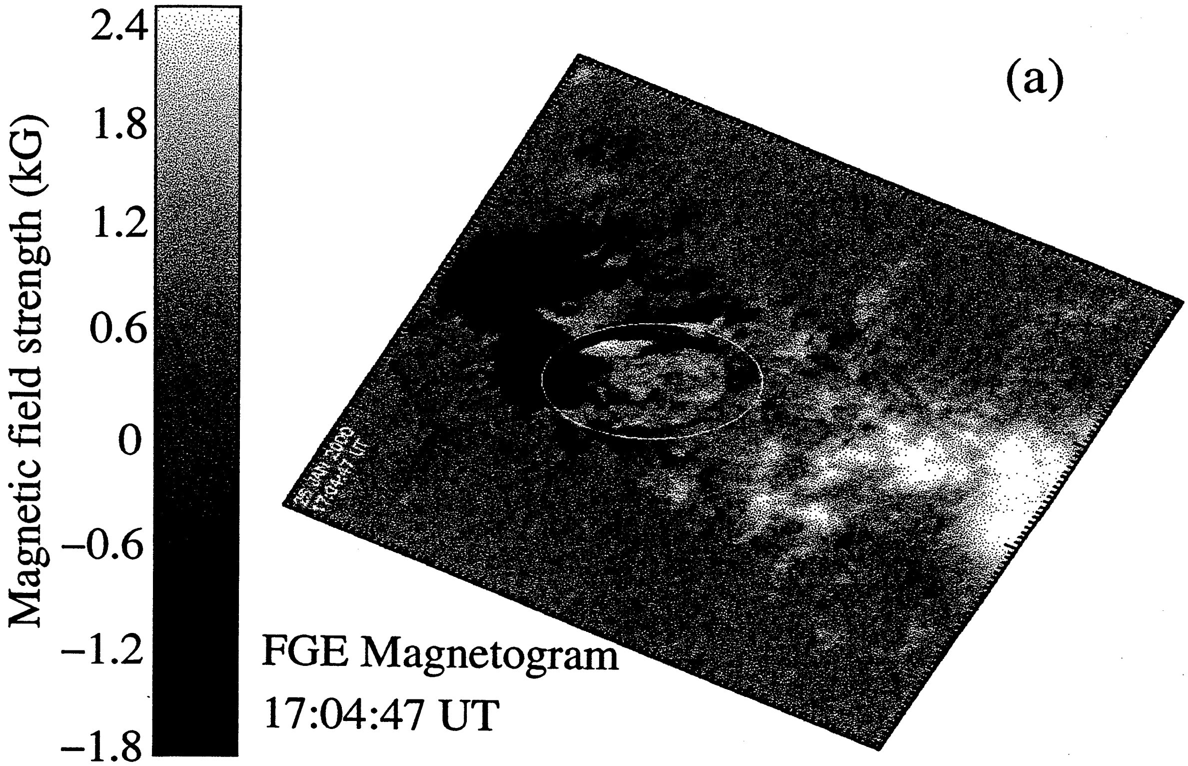
2.4
1.8
1.2
0.6
0
−0.6
−1.2
−1.8
Magnetic field strength (kG)
(a)
25 JAN 2000
17:04:47 UT
FGE Magnetogram
17:04:47 UT

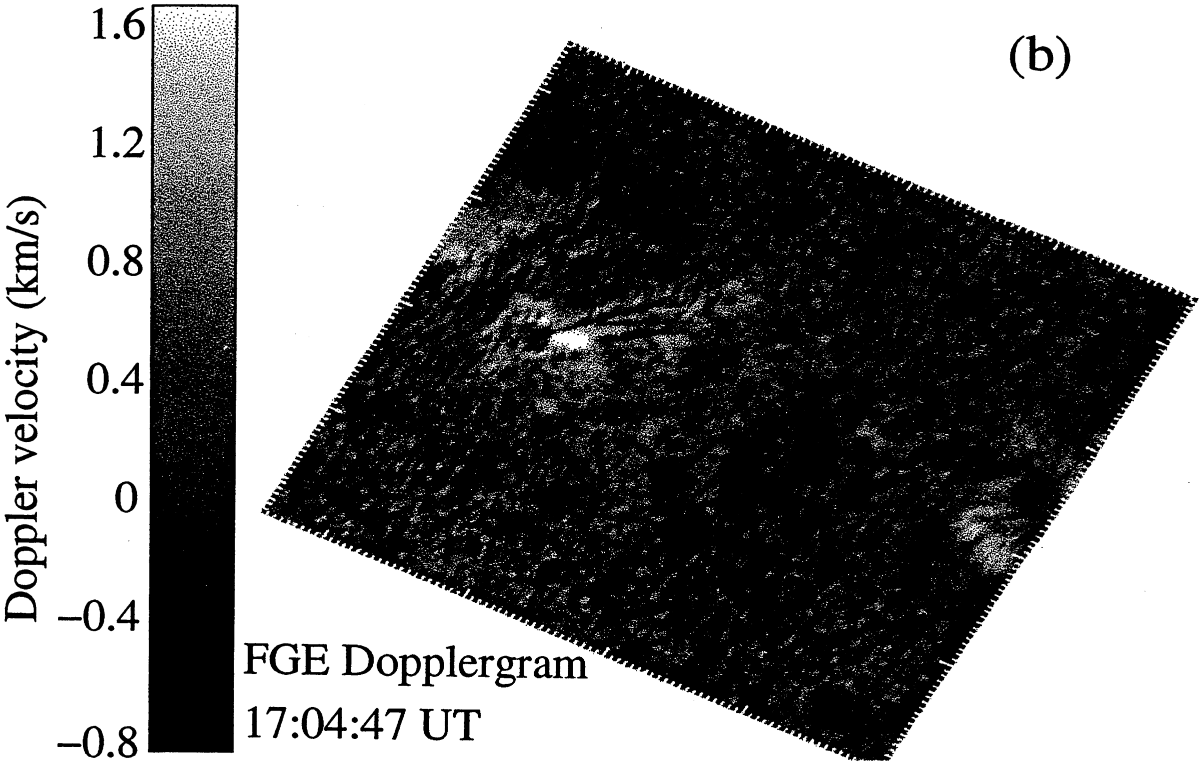
1.6
1.2
0.8
0.4
0
−0.4
−0.8
Doppler velocity (km/s)
(b)
FGE Dopplergram
17:04:47 UT

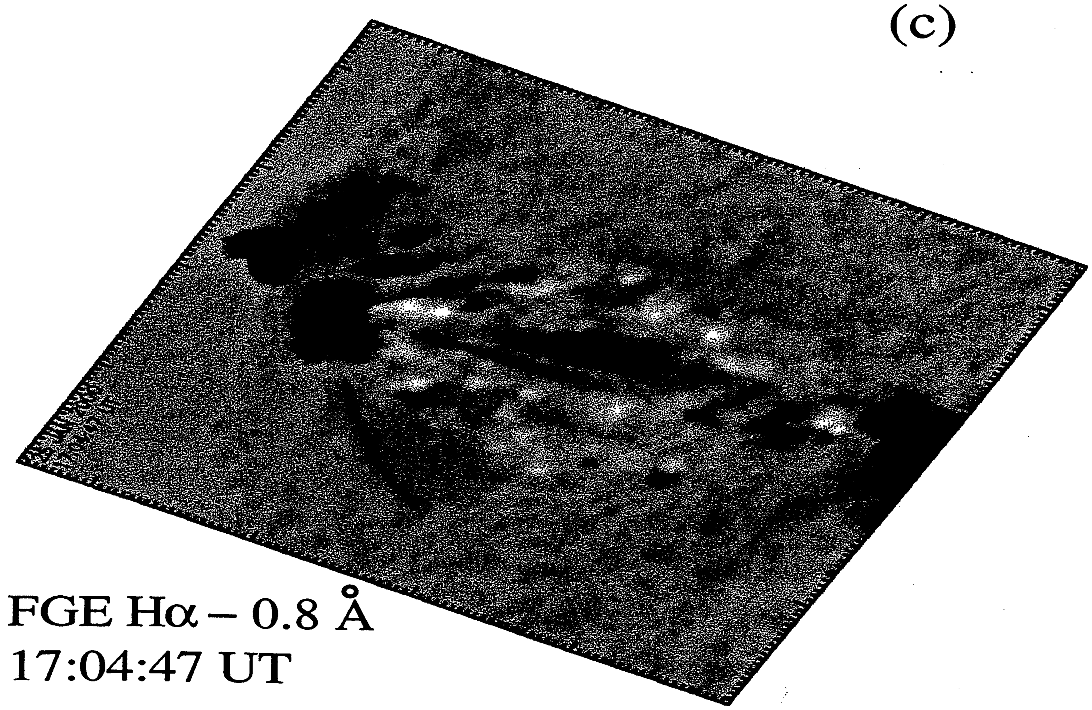

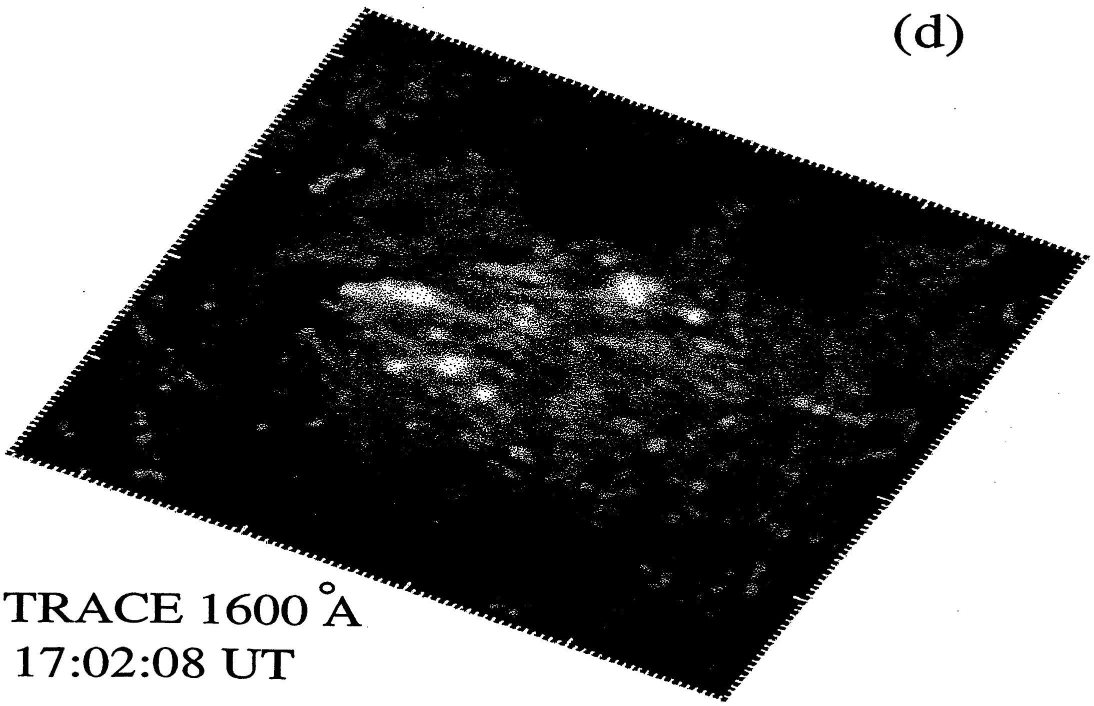

Fig. 1.— Four nearly simultaneous views of the AR NOAA 8844 on January 25, 2000, obtained by the FGE: (a) LOS longitudinal photospheric magnetogram. Bright/dark patches indicate positive/negative polarity. The white ellipse encloses a supergranular cell, at the vicinity of the following sunspot. (b) Photospheric Doppler velocities. Bright/dark patches indicate upflows/downflows. c) $H\alpha - 0.8$ Å filtergram. A multitude of EBs may be seen as localized brightenings underneath the superposed AFS (elongated, dark fibrils). (d) UV 1600 Å continuum emission, obtained by TRACE. The tick mark separation in all images is 1 *arcsec*. North is up; west is on the right.

The co-alignment of the TRACE 1600 Å images with the FGE data was accomplished in two stages: First, by aligning the position of the sunspots in both wavelengths and, second, by aligning small-scale features, visible in both wavelengths. To map the transverse velocity field on the photospheric level (proper motions), we have applied a cross-correlation tracking technique to FGE white light images (R. A. Shine, 2001, private communication).

A set of nearly simultaneous views of AR NOAA 8844 is shown in Fig. 1. A typical LOS photospheric magnetogram is shown in Fig. 1a. The photospheric Doppler velocity map in shown in Fig. 1b. The simultaneous $H\alpha - 0.8$ Å filtergram is given in Fig. 1c. Notice the numerous EBs beneath the AFS (dark elongated structures extending between the two sunspots). EBs are visible as localized enhancements of $H\alpha - 0.8$ Å emission. In Fig. 1d, the simultaneous 1600 Å continuum image of the T_{min} region is given. Localized enhancements of emission are also abundant here. We will, hereafter, refer to these transients as 1600 Å BPs. Besides BPs in Fig. 1d, we also obtain bright, elongated structures in the interspot area. We believe that these fibril structures originate from emission in the C IV line (1550 Å). This emission is beyond the scope of the present study.

Figure 1 shows that the emergence of magnetic flux in the AR is an asymmetric process. The preceding sunspot (positive polarity) is more compact than the trailing sunspot (negative polarity), which appears less organized and more fragmented. Westward motions at the vicinity of the leading spot are more systematic compared to those at the vicinity of the following spot, where we notice a small (~ 15 *Mm*) supergranular cell (enclosed by the ellipse in Fig. 1a). We will not deal with these asymmetries in this work, but one may refer to the works by van Driel-Gesztelyi and Petrovay (1990), Petrovay et al. (1990), and Fan, Fisher, & DeLuca (1993).

3. Occurrence Rates and Spatial Distribution of EBs

To identify individual EBs, we rely on the contrast $I_c(\mathbf{x},t) = \frac{I(\mathbf{x},t)-I_0}{I_0}$, calculated for each location in the $H\alpha - 0.8$ Å filtergrams. Here $I(\mathbf{x},t)$ is the intensity of a pixel with vector position $\mathbf{x}$ at time t and I_0 is the background (mean) intensity for all frames and for the entire observing time. Setting all pixels with contrast fainter than some predefined value to zero, we obtain "islands" of enhanced $H\alpha - 0.8$ Å emission, which correspond to EBs.

To track the temporal evolution of EBs we assume that an EB, identified in one frame, survives to the next frame if there is a spatial overlapping of at least one pixel between islands of enhanced $H\alpha - 0.8$ Å emission in two consecutive frames. This somewhat crude rule may underestimate the total number of EBs and overestimate EB lifetimes because: *(i)* Experiments with better cadence report EB lifetimes of the order of a few *min*, which is less than our cadence. The tendency of EBs to recur at the same locations may, therefore, lead to undetected EB recurrence. *(ii)* Depending on the local proper motions, an EB may migrate to the location of a pre-existing EB which may have faded between frames. We have created an algorithm that automatically identifies EBs and tracks their evolution in time. According to the algorithmic rules, *(i)* two EBs that merge are, thereafter, treated as one event, and *(ii)* an EB that splits in two or more separate emission kernels is still treated as one EB and is considered terminated only when the last remaining kernel fades below background.

The results of the above selection process are the following:

The observed contrasts of EBs vary in the range [0.05, 0.30], that is, 5% to 30% above the background. The average contrast, calculated for all pixels over the entire observing time, is $\sim$ 0.08. This average is significantly lower compared to previous reports. Zachariadis, Alissandrakis, & Banos (1987) reported an average contrast of $\sim$ 27% , while Nindos & Zirin (1998) reported a mean value of $\sim 29 - 31\%$. We have defined several contrast thresholds, or background contrasts, in the range [0.05,0.20]. The total number of EBs varies between 593 events (for a background contrast $I_{c_0} = 0.05$) and 29 events (for $I_{c_0} = 0.20$). For $I_{c_0} = 0.08$, close to the average contrast, we identified 295 EBs. The total observing time being $\sim$ 206 *min* and assuming a smooth, uninterrupted EB production,we find that the mean occurrence rate of EBs varies in the range

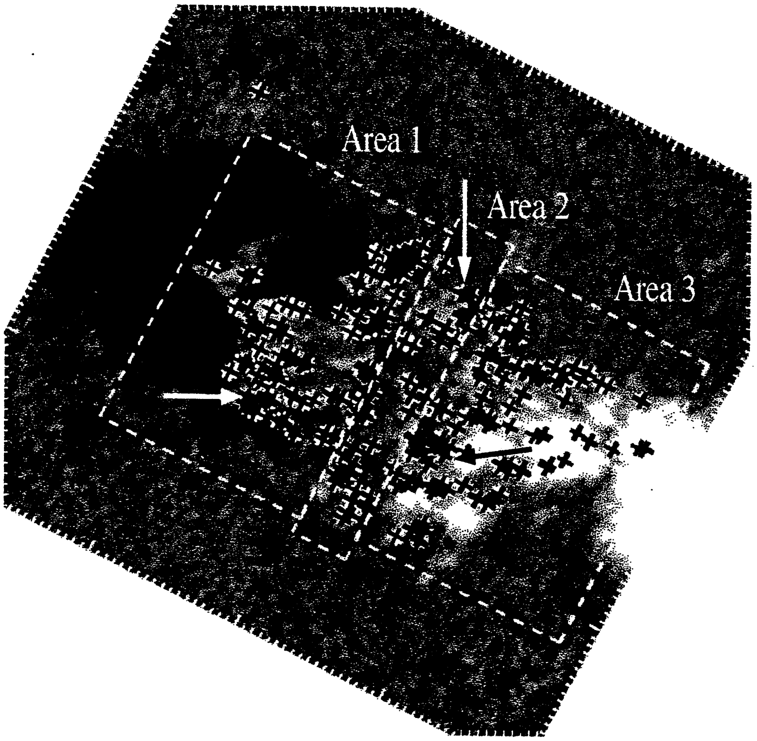

Fig. 2.— The mean origin locations of EBs (crosses) obtained using a background contrast $I_{c_0} = 0.08$ (295 events). A typical LOS longitudinal magnetogram is shown in grayscale. Bright/dark patches indicate positive/negative polarity. The EB-producing area has been divided in three parts (for details, see text). The three arrows indicate the locations of the EB examples shown in Fig. 5, one for each of the designated areas 1, 2, and 3. The tick mark separation is 1 *arcsec*. North is up; west is on the right.

[0.14, 2.88] EBs min^{-1}, for an EB producing area $\sim$ 1800 $arcsec^2$. For $I_{c_0} = 0.08$, the mean occurrence rate is $\sim$ 1.43 EBs min^{-1}. The above occurrence rates for a given background contrast should be considered as lower limits of the actual occurrence rates, since *(i)* our results may be systematically biased due to the moderate cadence, compared to typical EB lifetimes, and *(ii)* EBs occurring directly underneath the AFS's dark fibrils are obscured by the large-scale structure.

In Fig. 2 we show the mean locations of origin for the 295 EBs detected for $I_{c0} = 0.08$. A typical LOS longitudinal magnetogram is the grayscale background. It is clear from Fig. 2 that EB production is inhomogeneous and enhanced at:

(1) The boundaries of the supergranular cell, at the vicinity of the following sunspot (area 1). The supergranular boundaries are covered by EBs, while EB density is significantly lower in the interior of the supergranule. The boundaries of the cell are sustained by converging proper motions, of the order (0.2, 0.5) $km\ s^{-1}$, and they are dominated by downflows in the range (−0.4, −0.1) $km\ s^{-1}$. In the supergranular interior, EBs are mostly associated with small-scale moving dipolar (magnetic) features (MDFs) which drift toward the following sunspot, or toward the cell boundaries, with velocities in the range (0.7, 1) $km\ s^{-1}$. MDFs found in the FGE data are peculiar moving magnetic features and are studied separately by Bernasconi et al. (2002).

(2) The polarity reversal area (area 2). EBs observed in this area of intense flux emergence are often associated with small-scale MDFs (Bernasconi et al. 2002) moving with velocities of the order (0.3, 0.8) $km\ s^{-1}$.

(3) The vicinity of the leading sunspot (area 3). This area is mostly unipolar and characterized by systematic proper motions of newly emerged magnetic fields of positive polarity toward the sunspot. Proper motions are of the order (0.6, 0.8) $km\ s^{-1}$ and the moving patches correlate with downflows $\sim -0.5\ km\ s^{-1}$. Notice that the origin locations of EBs form chains that lead to the preceding sunspot. These chains correlate well with the paths of the above-mentioned moving bundles of magnetic flux.

Our results are in agreement with previous studies reporting that the spatial distribution of EBs is not random or homogeneous (Vorpahl and Pope 1972; Bruzek 1972; Zachariadis, Alissandrakis, & Banos 1987). A detailed study of the photospheric patterns for each of the three areas shown in Fig. 2, follows in § 4.2.

4. Morphology and Characteristics of EBs

4.1. Typical size and the degree of elongation

Previous works (Kurokawa et al. 1982; Nindos and Zirin 1998) reported that EBs are elongated structures with their length typically 37% - 45% larger than their width. To investigate this, we selected five representative background contrasts I_{c_0}, namely, 0.05, 0.08, 0.12, 0.16, and 0.20 and we inspected visually the shapes of the most conspicuous EBs for each case. We measured the sizes of 328 EBs (165 for $I_{c_0} = 0.05$, 103 for $I_{c_0} = 0.08$, 40 for $I_{c_0} = 0.12$, 15 for $I_{c_0} = 0.16$, and 5 for $I_{c_0} = 0.20$). The main/secondary axis of the examined EBs was called the length/width of the EBs. Knowledge of the length l and the width w of an EB allows the calculation of the *degree of elongation* e, defined as $e = \frac{l-w}{l} \times 100$. From this definition, $e = 0\%$ for a circle and $e \sim 100\%$ for $l \gg w$.

In Fig. 3 we show the average degree of elongation for all five definitions of the background.

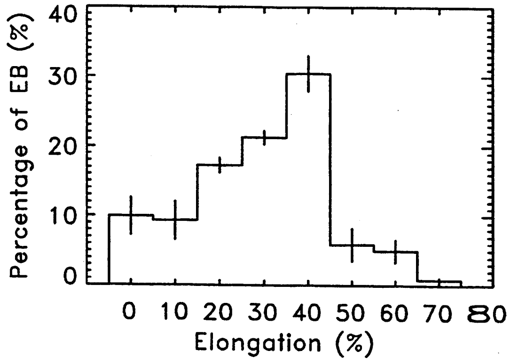

Fig. 3.— Histogram of the measured degree of elongation for well-defined EBs obtained with background contrasts $I_{c_0} = 0.05, 0.08, 0.12, 0.16$ and 0.20. Also shown, with error bars, is the standard deviation for each EB percentage associated with a certain degree of elongation.

The histogram was created using 8 equal elongation bins of width 10%. The measured degree of elongation is located at the center of each bin while the error bars correspond to the standard deviation for each EB percentage associated with a degree of elongation. From Fig. 3 we conclude that *(i)* EBs are elongated structures, but there is an upper limit for the degree of elongation and *(ii)* there exists a preferential degree of elongation. Roughly 10% of EBs are circular structures ($e \simeq 0$), while for 75% of EBs we obtain 10%< e < 40%. For nearly half of the elongated EBs we obtain $e \simeq 40\%$, that is, their length is 40% larger than their width. This is the preferential degree of elongation, even given the error bars. This degree of elongation is in close agreement with previous results. For about 15% of EBs we obtain $e > 40\%$, while no EB exhibits a degree of elongation larger than $\sim 70\%$. We conclude that EBs are mostly elongated structures, but only rarely (if at all) does the degree of elongation exceed 60%.

The mean EB sizes, on the other hand, can be estimated by more than one way:

(a) By directly measuring EB sizes. This method is biased in favor of the most conspicuous EBs, since the measurements cannot be reliable for EBs with sizes close to the spatial resolution. Small EBs, consequently, have to be excluded and the mean EB sizes are calculated from only a fraction (less than 50%) of the total event sample.

(b) By calculating EB sizes. Using the preferential degree of elongation, we assume that $l \simeq 1.67w$ and that EBs are elliptical structures. We then obtain $w \simeq \sqrt{\frac{S}{1.67\pi}}$, where S is the measured EB area. This set (l, w) of EB dimensions can be viewed as the anticipated dimensions of an EB which extends over an area S.

We noted in § 3 that the average contrast of our EBs is ~ 0.08. Let us use this background ($I_{c_0} = 0.08$) in order to determine the mean EB sizes. By directly measuring the EB sizes, that is, by using 103 events out of a total of 295 EBs, we obtain average EB sizes of the order 2.5×1.7 *arcsec*^{2}. Assuming $l \simeq 1.67w$, we use the entire EB sample to obtain an average size of the order 1.8×1.1 *arcsec*^{2}, using the measured EB areas. The mean EB dimensions are not much larger than our spatial resolution (~ 0.8 *arcsec*). Improved spatial resolution will, probably, result in even smaller "typical" EB sizes. This is an indication that finite spatial resolution precludes a detailed analysis on EB sizes and that probably many EBs remain undetected. This assertion is further supported by the significantly larger average contrast in $H\alpha - 0.8$ Å within the EB-producing area (Fig. 1c), excluding EBs, compared to the average contrast of the quiescent areas on both sides of the interspot region. Moreover, we will show in §5.2 that there is a strong positive correlation between the size (area) and the peak intensity of EBs, indicating clearly that fainter EBs occupy smaller areas.

4.2. The photospheric signature of EBs

The photospheric conditions that give rise to EB occurrence are less than clear. Topics to be addressed include the association of EBs with neutral lines of the longitudinal photospheric magnetic field, photospheric Doppler motions, and the proper motions of EBs. In the following analysis we investigate the correlations of EBs with the underlying photospheric pattern. We will, again, use a background contrast $I_{c_0} = 0.08$, close to our average EB contrast.

We first study the association of EBs with photospheric neutral lines of the LOS longitudinal magnetic field. In this analysis we do not use the tracking algorithm of EBs in time, since the process would then become very complicated. Instead, we examine each $H\alpha$ filtergram, counting each EB as a different case. Consequently, we examined 173 EBs in area 1, 172 EBs in area 2, and 340 EBs in area 3. Our results suggest that the presence of photospheric neutral lines is not a prerequisite for EB triggering. Area 1 is dominated by persistent neutral lines that outline the supergranular boundary. Since these boundaries are areas of enhanced EB production, a decisive majority of EBs (77%) is found to occur above neutral lines. This percentage includes EBs that occur above the neutral lines of MDFs in the supergranular interior. Area 2 is the polarity reversal area of the AR. The majority of EBs found in this area (65%) also occur above neutral lines of the newly emerged magnetic flux. These lines are not as well-defined as the neutral lines in area 1, because magnetic fields are weaker in area 2. In some cases, we see EBs occurring above small-scale MDFs. Area 3, on the other hand, is mostly unipolar. Nonetheless, this area also produces a large number of EBs. Only 36% of these EBs correlate with photospheric neutral lines, while the majority of EBs (64%) occur in unipolar areas.

Next, we investigate the proper motions of EB loci. To measure these horizontal velocities, we calculate the mean locations (centroids) of EBs for the first and the last frame in which they appear. The mean velocity of an EB loci, then, is the ratio of the distance covered by the EB's centroid over the elapsed time between the initial and the final frame in which the EB was detected.

Our results suggest that the supergranular boundaries (area 1) trigger numerous EBs that are mostly short-lived and their loci do not travel significant distances. The calculated proper motions do not exceed 0.4 $km\ s^{-1}$, while, in most of cases, they are less than 0.2 $km\ s^{-1}$. In the supergranular interior the situation is different, with a few EBs (associated with MDFs) showing proper motions in the range $(0.4, 0.8)$ $km\ s^{-1}$, or even exceeding 0.8 $km\ s^{-1}$. The polarity reversal area (area 2) produces EBs with typical loci proper motions in the range $(0.2, 0.4)$ $km\ s^{-1}$.

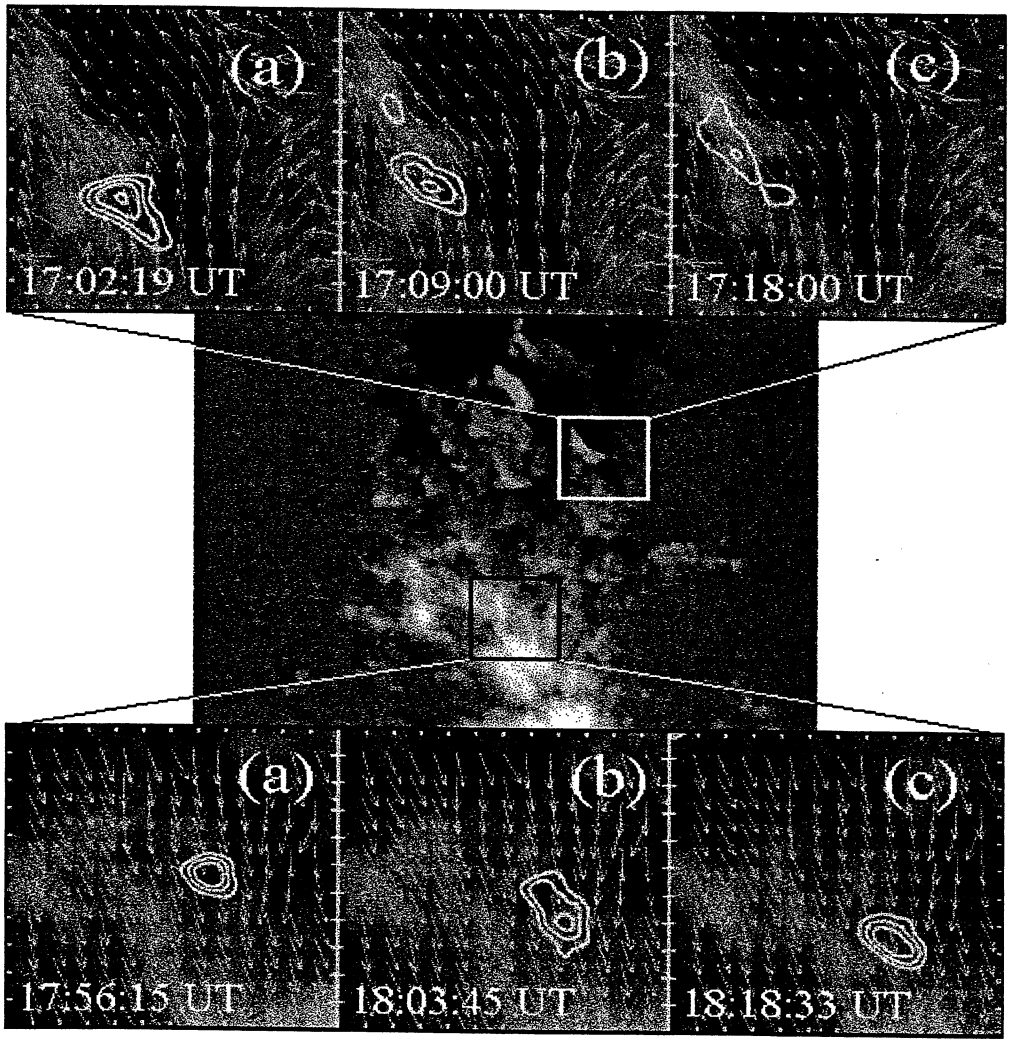

Fig. 4.— Two examples of EB proper motions in area 1 (white rectangle) and in area 3 (black rectangle). The evolution of EBs in three consecutive frames, labeled (a), (b), and (c), is shown. The un-scaled image is a typical LOS longitudinal magnetogram. The enlarged areas include the LOS longitudinal magnetic field in grayscale, the EB contrast (contours), and the average proper motions (vector field), calculated by correlation-tracking techniques. Tick mark separation in the magnification is 1 *arcsec*. The upper area (white rectangle) includes a strong neutral line, while the lower area (black rectangle) is mostly unipolar. The EB locus in area 1 moves with a velocity $\sim 1.15\ km\ s^{-1}$, whereas the EB locus in area 3 moves with velocity $\sim 1.35\ km\ s^{-1}$. The UT times are shown at the left corner of the enlarged images.

Slow-moving EBs (with velocities $< 0.2\ km\ s^{-1}$) were also found. In only one case do EB proper motions exceed $0.4\ km\ s^{-1}$ in area 2. The vicinity of the leading polarity (area 3), on the other hand, produces a large number of EBs with loci showing significant proper motions. The typical velocity range is $(0.4, 0.6)\ km\ s^{-1}$. Fast motions, of the order $(0.6, 0.8)\ km\ s^{-1}$, were found in some cases. Several EBs move with velocities $< 0.2\ km\ s^{-1}$, while very few EBs show velocities that exceed $0.8\ km\ s^{-1}$.

EB loci appear to follow the transverse photospheric mass flows. This is more definitive in the areas of systematic horizontal flows, i.e., the supergranular area and the unipolar vicinity of the leading sunspot. We depict two examples in Fig. 4. Two parts of the field of view have been enlarged, in area 1 and in area 3, respectively. In the expanded images, we depict the LOS longitudinal magnetic field (grayscale), the EBs (contours) and the average proper motions (vector field). Three frames, labeled (a), (b), and (c), show the temporal evolution of EBs, in both examples. Clearly, the EBs, or at least the EB loci, appear to follow the photospheric flow pattern.

Let us now study the association of EBs with the LOS longitudinal velocity of the photospheric magnetic fields (Fig. 1b). Before describing the results, it is useful to give the overall picture of the Doppler motions in the AR. Flux emergence is asymmetric, as noted in § 2. The sunspots are mostly associated with upflows. In the leading spot, ascending motions span in the range $(0.1, 0.4)\ km\ s^{-1}$, whereas in the following spot we obtain intense upflows of the order $(0.2, 1.0)\ km\ s^{-1}$. No preferential longitudinal motions of magnetized plasma are detected in the polarity reversal area. Doppler velocities vary in the range $(-0.3, 0.3)\ km\ s^{-1}$. Persisting downflows, on the other hand, can be found *(i)* at the supergranular boundaries, with motions of the order $(-0.4, -0.1)\ km\ s^{-1}$, and *(ii)* at the locations of the moving unipolar magnetic patches, in area 3. Doppler velocities in this area are $\sim -0.5\ km\ s^{-1}$.

To associate EBs with the photospheric Doppler motions, we performed a similar analysis as in the case of EB association with neutral magnetic lines. We find that almost all EBs are associated with photospheric downflows. In area 1, we find that photospheric downflows accompany 86% of EBs. The respective percentages are 86% for area 2 and 81% for area 3. Notice the similar percentages in all areas of the AR. This behavior is not seen either in the association of EBs with neutral lines or in the proper motions of EB loci. Different areas of the AR give different results, in both cases. We need to clarify that, to find the percentage of EBs associated with downflows in area 1, some further considerations were made. For several EBs in area 1 the Doppler signal was blue-shifted. However, in most of these cases, the Doppler velocity exhibited a *local minimum* in absolute magnitude (examples are given in § 4.4). These relative downflows in the locations of EBs, with respect to the EBs' surroundings, may be either due to LOS viewing angle problems, or due to small-scale, unresolved downflows superposed to macroscopic upflows. In area 1, 46% of EBs are associated with downflows and 40% of EBs correlate with upflows showing a clear velocity minimum in the EB location. Adopting the above interpretation, the percentage of EBs that correlate with downflows in area 1 is 86%, as mentioned above. Local minima of upward Doppler velocity are seen for 6% of EBs in area 2 and for 1 % of EBs in area 3. The majority of EBs in these areas, however, are associated with actual downflows.

An interesting feature of EBs in area 3 is that they occur in unipolar areas. These EBs are triggered above the *leading edges* of rapidly moving, recently emerged magnetic flux bundles. We conclude that these EBs occur in locations of interaction between the pre-existing magnetic field lines and the newly emerged magnetic flux. As we will show in § 4.4, the interacting magnetic configurations have different *geometries*. Parts of the pre-existing magnetic field are relatively horizontal, while the moving magnetic patches form large angles with the horizontal plane. The proper motions of these patches force the different magnetic configurations to interact, producing swarms of EBs. Examples are given in § 4.4 (Figs. 6 and 7) and we attempt to interpret this interesting result in § 7.

4.3. EB association with 1600 Å BPs in the temperature-minimum region

In Severny (1968), and in references therein, EBs are classified as photospheric entities. Re-

	Magnetic neutral lines	Proper motions of EB loci	Downflows	1600 Å BPs
Area 1.........	77%	$(< 0.2 - 0.4)$ $km\ s^{-1}$ (supergranular boundary) $(0.4 - > 0.8)$ $km\ s^{-1}$ (cell interior/MDFs)	86% $(-0.4, -0.1)$ $km\ s^{-1}$	54%
Area 2.........	65%	$(< 0.2 - 0.4)$ $km\ s^{-1}$	86% $(-0.3, -0.1)$ $km\ s^{-1}$	56%
Area 3.........	36%	$(< 0.2 - 0.8)$ $km\ s^{-1}$	81% ~ -0.5 $km\ s^{-1}$	55%

Table 1: Synoptic results on the association of EBs with the underlying photospheric pattern (magnetic fields and mass flows) and the association of EBs with 1600 Å BPs in the T_{min} region.

cently, however, it has been conjectured that EB emission originates from close to the T_{min}, at a height 600 km - 1100 km above the $\tau_{5000} = 1$ layer (Payne 1993). BPs in 1600 Å are a typical feature of the T_{min}, occurring due to the ionization of Si and Fe in wavelengths 1500 – 1680 Å (Vernazza, Avrett, & Loser 1981). Qiu et al. (2000) reported that $\sim 61\%$ of their EBs correlate with 1600 Å BPs.

From the 13 TRACE frames at 1600 Å that are nearly simultaneous with FGE $H\alpha$ filtergrams, we visually examined 448 EBs (142 EBs in area 1, 106 EBs in area 2, and 200 EBs in area 3) and their association with 1600 Å BPs. In agreement with Qiu et al. (2000), we found that slightly more than half EBs are associated with 1600 Å BPs, independently of the area. In 54%, 56%, and 55% of EBs from area 1, area 2, and area 3, respectively, a clear correlation with 1600 Å BPs could be seen. These percentages should be considered average, however, since the association of EBs with BPs depends on the size of the EBs. For bright and persistent EBs the percentage exceeds 90%, but it can be as low as 45% for faint, short-lived EBs. We noticed an interesting property of EBs associated with MDFs in the supergranular interior. Although these EBs typically persist for as long as the MDFs are visible, no 1600 Å BPs appear related to them.

Our results are in agreement with the results of Qiu et al. (2000). An interesting open problem is to determine which emission ($H\alpha$ or UV) precedes the other. Unfortunately, our moderate cadence does not allow such an investigation. The photospheric conditions beneath EBs, as well as the association of EBs with 1600 Å BPs, are summarized in Table 1.

4.4. Some representative EB cases

In Fig. 5 we depict three EB examples (one for each of the areas 1, 2, and 3). $H\alpha - 0.8$Å emission is outlined by the thick, solid contours, while the thick dashed contours outline 1600 Å BPs. The grayscale background corresponds to both the LOS longitudinal magnetic field (left column; images labeled (a)) and the Doppler velocity (right column; images labeled (b)). Dark patches correspond to vectors oriented downwards, while bright patches correspond to vectors pointing upwards. The thin solid contours represent neutral magnetic lines (left column) and zero-velocity lines (right column).

In all cases, EBs are clearly associated with 1600 Å BPs. The EB from area 1 (upper row) occurs above a well-defined neutral line and an area of photospheric downflows. The EB from area 2 (middle row) also correlates with a magnetic neutral line. This line is more noisy compared to the one shown in the upper row, since magnetic fields in area 2 are typically weaker compared to those found in area 1. The EB is, again, associated with photospheric downflows. The EB from area 3 (lower row) clearly occurs in the absence of neutral magnetic lines, in a unipolar area of positive polarity. Nevertheless, this EB is also associated with photospheric downflows.

In Fig. 6 we show two examples of EBs for each of the areas 1, 2, and 3. We have now defined

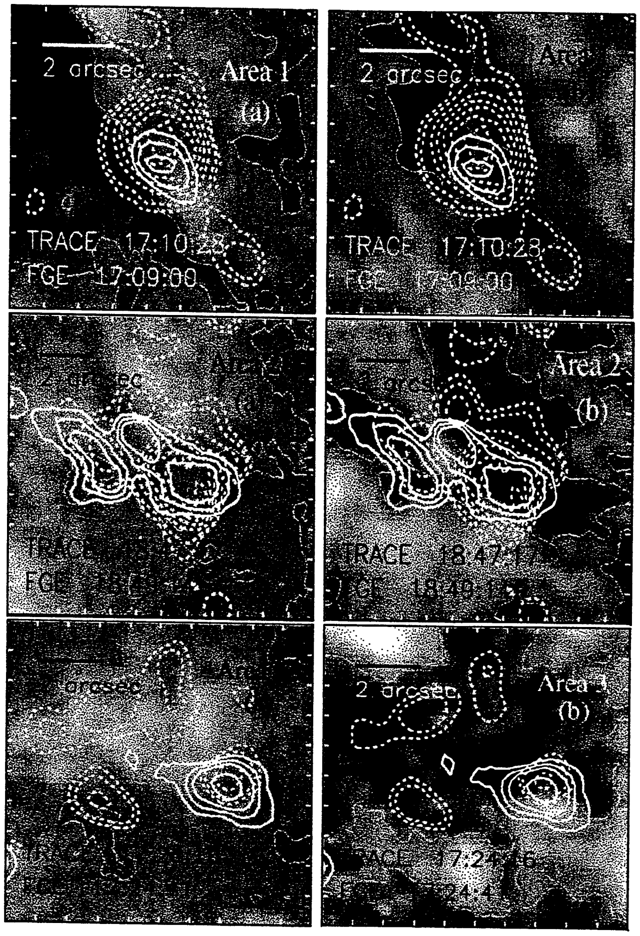

Fig. 5.— Three examples of EBs and their local conditions. The locations of enhanced $H\alpha - 0.8$ Å emission are shown by thick solid contours. Enhanced UV 1600 Å continuum emission is indicated by dashed contours. The grayscale backgrounds correspond to the (nearly) simultaneous LOS longitudinal magnetic field (left column; cases labeled (a)) and Doppler velocity (right column; cases labeled (b)). Each EB is plotted twice in each row using the above-mentioned backgrounds. The thin solid line indicates neutral magnetic lines (left column) and zero-velocity lines (right column). The tick mark separation is 1 *arcsec*. The UT times of the observations are shown at the lower left corner of the images, for the $H\alpha - 0.8$ Å filtergrams (FGE) and the UV images (TRACE). The exact locations of the EBs in the AR are indicated by arrows in Fig. 2.

a number of one-dimensional spatial profiles (line-cuts) and we depict the evolution of various parameters along the selected line segments. Information includes the $H\alpha - 0.8$ Å contrast (thick solid line), the 1600 Å contrast (dash-dotted line), the LOS longitudinal magnetic field (thin solid line), and the Doppler velocity (dashed line). The background for the $H\alpha$ and the UV emission is set to zero.

The EB in Fig. 6a is associated with both a well-defined neutral magnetic line (separating magnetic fields $\sim$ 500 G and $\sim$ -1000 G) and a 1600 Å BP. The Doppler motions are ascending. However, there is a local velocity minimum of $\sim$ 0.1 $km\ s^{-1}$ roughly coinciding with the EB, whereas the Doppler velocity in the surrounding areas is as high as 1 $km\ s^{-1}$. In Fig. 6b, the brighter EB is associated with a downflow $\sim$ -0.5 $km\ s^{-1}$, a neutral magnetic line and a 1600 Å BP. In area 2 (Figs. 6c, d), both the magnetic fields and the Doppler motions are weaker,

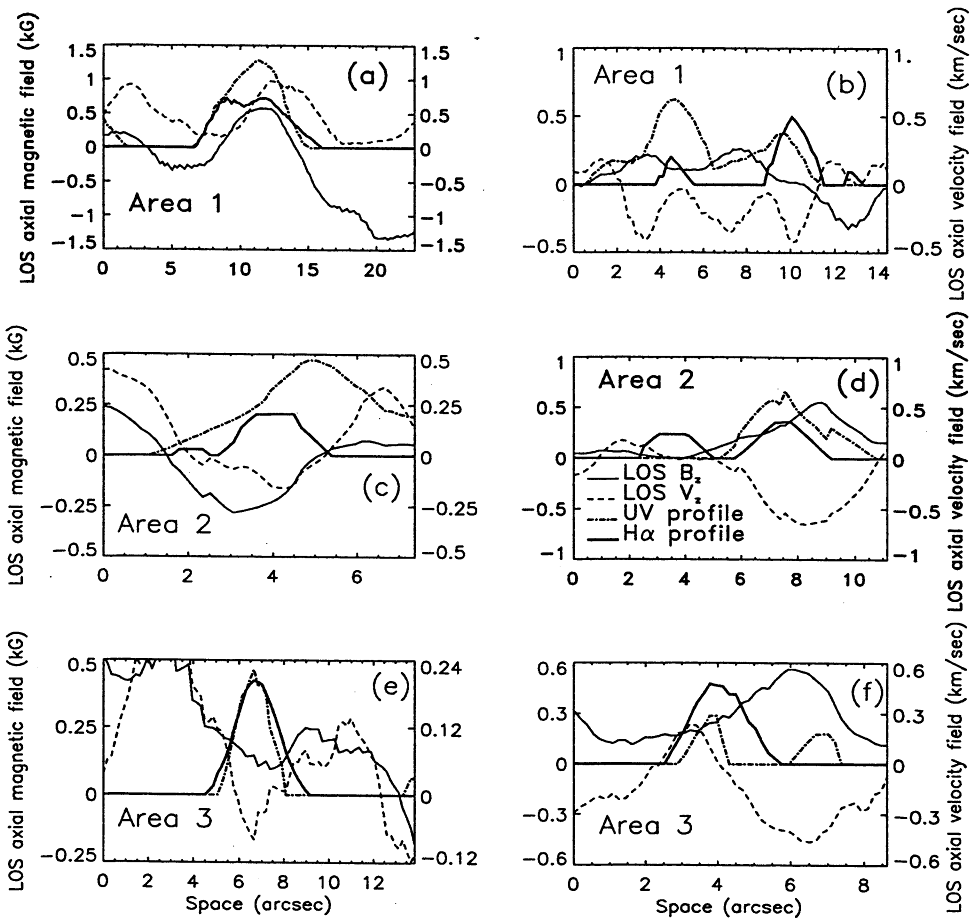

Fig. 6.— Six examples of one-dimensional spatial profiles of EBs. The information along the line is the $H\alpha - 0.8$ Å contrast (thick solid curves), the UV 1600 Å contrast (dash-dotted curves), the LOS longitudinal magnetic field (thin solid curves) and the Doppler velocity (dashed curves). A legend is given in diagram (d), for reference. Each curve is the average of 10 similar curves obtained from respective line-cuts. The line-cuts are parallel and uniformly distributed. The distance between adjacent line-cuts is equal to the pixel size.

compared to those of area 1. In Fig. 6c, a rather faint neutral line exists beneath the EB. The Doppler velocities, however, show a more profound behavior, reaching values ~ -0.15 $km\ s^{-1}$ beneath the EB. At the EB's surroundings, Doppler velocities are of the order 0.4 $km\ s^{-1}$. No neutral line can be seen in Fig. 6d, for both EBs. The fainter EB is not associated with a downflow or a 1600 Å BP, but a strong downflow of ~ -0.6 $km\ s^{-1}$ and a 1600 Å BP correlate nicely with the brighter EB. In Figs. 6e, f (area 3), the longitudinal magnetic field is clearly unipolar. A downflow of the order -0.1 $km\ s^{-1}$, however, occurs beneath the EB of Fig. 6e, while the surroundings of the EB show upflows of the order $(0.12, 0.24)$ $km\ s^{-1}$. The EB coincides precisely with a UV BP. In Fig. 6f one notices two 1600 Å BPs but only one EB. The EB occurs above the edge of an area dominated by descending motions of the order -0.5 $km\ s^{-1}$.

In Figs. 7a, b we use the same line-cuts as in Figs. 6e, f, respectively. The information shown here, however, is the $H\alpha - 0.8$ Å contrast (solid lines) and the zenith angle θ of the photospheric magnetic field vector with respect to the LOS di-

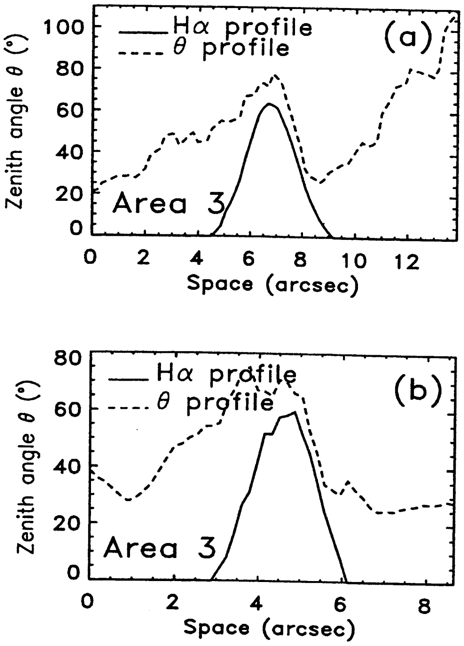

Fig. 7.— One-dimensional spatial profiles for the EBs of the last two examples of Fig. 6. The EBs from Figs. 6e and 6f are the same with the EBs of the diagrams (a) and (b), respectively. The information along the line is the $H\alpha - 0.8$ Å contrast (solid curves) and the zenith angle of the magnetic field vector (dashed curves). The orientation of motion of the relatively vertical magnetic flux bundles against the relatively horizontal, pre-existing field, is from right to left.

rection (dashed lines). θ ranges between 0^o (the magnetic field vector points outwards, along the LOS axis) and 180^o (the magnetic field vector points inwards). For $\theta \simeq 90^o$ the magnetic field vector is nearly transverse to the LOS axis. From Fig. 7 we find that there is a steep gradient of the zenith angle in the locations of EBs. The newly emerged magnetic patches which drift toward the leading sunspot in area 3 are mostly perpendicular to the photosphere ($25^o \leq \theta \leq 30^o$) and they interact with the mostly horizontal, pre-existing magnetic fields ($70^o \leq \theta \leq 80^o$). Therefore, in both examples of Fig. 7, EBs occur where relatively vertical magnetic fields are interacting with pre-existing, relatively horizontal, fields.

5. The statistical properties of EBs

5.1. The fractal character of EB clusters

Let us now investigate statistically the spatial distribution of EBs. A first-order approach to tackling this problem is the investigation of the fractal character of EB occurrence. For large-scale structures, the numerical calculation of the fractal dimension provides information on the degree of complexity that characterizes the structures' boundaries. For small-scale structures, occurring in swarms and having sizes comparable to the spatial resolution, the fractal dimension provides insight on how inhomogeneous the clustering process of these structures is. This information will be provided for EBs, since EBs meet the second type of conditions.

To calculate the fractal dimension, we rely on a two-dimensional box-counting method (for a complete description see, e.g., Mandelbrot 1983 and references therein) as follows: We cover each $H\alpha - 0.8$ Å frame with a two-dimensional, uniform, rectangular grid, consisting of boxes with size $\lambda \times \lambda$. If our field of view has a size $L \times L$, then it is covered by $(L/\lambda)^2$ boxes with a non-dimensional area ε^2; $\varepsilon = \frac{\lambda}{L}$. The total number of boxes being $(L/\lambda)^2$, we count the number of boxes that enclose non-zero information, that is, at least one EB or a part of at least one EB's boundaries. If this number is $N(\lambda)$, we vary the box-size λ (or, equivalently, the non-dimensional box-size ε) and study the variability of $N(\lambda)$ vs. λ (or $\frac{1}{\varepsilon}$). For a fractal structure, one should obtain

$$N(\varepsilon) \propto (\frac{1}{\varepsilon})^{\mathcal{D}_0} \qquad (1)$$

where $\mathcal{D}_0$ is the (box-counting) fractal dimension. $\mathcal{D}_0$ can be at most equal to the embedded (Euclidean) dimension of the space, for non-fractal structures, or smaller, for fractal structures, but not larger than that. In our case, $\mathcal{D}_0 \leq 2$. $\mathcal{D}_0 = 2$ would imply a spatially homogeneous event distribution, whereas for $\mathcal{D}_0 \ll 2$ (and large statistical samples) events show a strong preference to organize in clusters.

An example of the numerical calculation of the fractal dimension is shown in Fig. 8a. Moreover, we have calculated the fractal dimension of EB

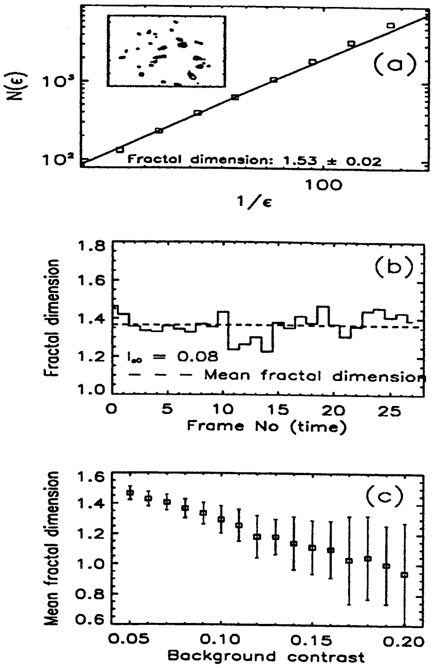

Fig. 8.— (a) Numerical calculation of the fractal dimension of EB clusters for a given frame (shown in the inset). The dynamical range over which the fractal dimension is estimated exceeds one order of magnitude. (b) The time variability of the fractal dimension of EBs for $I_{c_0} = 0.08$. The mean value of the fractal dimension (~ 1.4) is shown by the dashed line. (c) The mean fractal dimensions for different background selections. The error bars correspond to the standard deviation for each fractal dimension, as calculated by the square root of the variance in the time variability of the fractal dimension for a given background. Clearly, the standard deviation (or the variance) increases with increasing background. For $I_{c_0} > 0.11$ the calculation of the mean fractal dimension becomes unreliable, due to poor statistics.

clusters for all FGE $H\alpha$ -0.8 Å filtergrams, thus constructing the timeseries of the fractal dimension variations for different background contrasts in the range $(0.05, 0.20)$. We found that EB clustering is a fractal process, since we obtain a fractal dimension $\mathcal{D}_0$ between 1.5 (for $I_{c_0} = 0.05$) and 1.0 (for $I_{c_0} = 0.20$). Moreover, the fractal dimension does not change appreciably with time for a given background, provided that the number of EBs is large enough to allow a reliable calculation. Stated differently, the fractal dimension fluctuates around a mean value. We show this behavior in Fig. 8b, for $I_{c_0} = 0.08$. The mean fractal dimension is $\bar{\mathcal{D}}_0 \simeq 1.4$. Fig. 8c shows the average (over the observing time) calculated fractal dimensions for different backgrounds I_{c_0}. We find that the fractal dimension decreases with increasing I_{c_0}.

The above findings suggest, from a different perspective, that the spatial distribution of EBs is inhomogeneous and that preferential locations in the AR are prolific in EB production. As we know, these locations are the supergranular boundaries (area 1) and area 3, where new magnetic flux accumulates on the leading sunspot (Fig. 2). Secondary locations are the polarity reversal area and the supergranular interior. The relative constancy of the fractal dimension with time (Fig. 8a) indicates that the character of the clustering process does not change significantly within our observing interval. Changes in the fractal dimension with time, for a given background contrast, can be mostly attributed to the varying numbers of EBs in each filtergram. This behavior is, probably, expected because *(i)* the preferential locations of EB occurrence do not change within our observing time, and *(ii)* the timescale of flux emergence, which ultimately triggers EBs, is large compared to our observing interval. The decreasing mean fractal dimension with increasing background contrast is due to the significantly smaller EB numbers as the background increases. For as long the statistics are sufficient, i.e., for $I_{c_0} \lesssim 0.11$ (Fig. 8b), this result indicates an enhancement of the clustering process. For $I_{c_0} > 0.11$, the rapidly decreasing numbers of EBs make the calculation of the fractal dimension unreliable, as shown by the large error bars in Fig. 8b.

5.2. Definitions and statistical properties of typical EB parameters

In this analysis, we define an array of parameters that highlight different aspects of EB "size". The parameters to be defined are the area of EBs, the EB lifetime (duration), the maximum and the total integrated EB contrasts.

To account for finite resolution effects, since EBs have sizes close to the spatial resolution, we introduce the following correction: We assume that the peak contrast $I_p(t)$ of an EB, at a given frame (time) t, decreases as a gaussian function of the distance l from the location of the peak. The parameters of the gaussian may be then calculated, using the EB length $l(t)$, as deduced by the measured EB area, for a given background contrast I_{c_0} (Appendix). Then we calculate the corrected area $S(t)$ for which the intensity fades to the mean intensity I_0 (contrast equal to 0). This area is, thereafter, treated as the EB area at time t.

This being said, we define the following EB parameters:

(1) The *lifetime* D of EBs. This is estimated simply by the number of frames over which an EB persists, multiplied by the average elapsed time between frames ($\sim 7.5\ min$). We mentioned before that a calculated EB lifetime may be the cumulative result of more than one EBs that recur and that short-lived EBs may have been unaccounted for. For this reason, we will not pursue any robust conclusion based on EB lifetimes. We have chosen this parameter, however, because it is required for the definitions of the parameters that follow. The duration of EBs is the only EB parameter that remains unaffected by the gaussian correction.

(2) The *corrected maximum EB area* S_{max}. This parameter is provided by the maximum

$$S_{max} = max\{S(t'); t' = t, t+1, ..., t+D\} \tag{2}$$

of the corrected areas $S(t')$ over an EB's lifetime D. The corrected area $S(t)$ of an EB at time (frame) t is given by

$$S(t) = S_p(t)\frac{logI_p(t)}{log(I_p(t)/I_{c_0})} \tag{3}$$

with $I_p(t)$ and $S_p(t)$ being the maximum EB contrast and the measured EB area at time t. The derivation of equation (3) is provided in detail in the Appendix.

(3) The *corrected maximum integrated contrast* I_{max} of EBs. The spatially integrated contrast $I_s(t)$ of an EB, at a given time t, is provided by the integral

$$I_s(t) = \int_{S(t)} I(S,t)dS \tag{4}$$

where $I(S,t)$ is the contrast of the EB emission throughout the area $S(t)$. Applying the gaussian correction, we obtain the corrected integrated contrast

$$I_s(t) \simeq I_p(t)b\sqrt{\pi}\ erf(0.74S^{1/2}(t)/2b) \tag{5}$$

where $b^2 = \frac{0.37S(t)}{lnI_p(t)}$, $erf(x) = \frac{2}{\sqrt{\pi}}\int_0^x e^{-u^2}du$ is the error function of x, $I_p(t)$ is the measured peak EB contrast, and $S(t)$ is the corrected EB area, at time t. For the derivation of equation (5), see Appendix.

The corrected maximum integrated contrast is now given by the maximum

$$I_{max} = max\{I(t'); t' = t, t+1, ..., t+D\} \tag{6}$$

of the corrected integrated contrasts over the lifetime D of an EB. The maximum integrated contrast of an EB refers to the EB's peak activity and is insensitive to the recurrence effect. If multiple, co-spatial EBs, are detected as one event due to undetected recurrence, then I_{max} reflects the peak activity of the most prominent of them.

(4) The *corrected total integrated contrast* I_{tot} of EBs. This parameter occurs after integrating in time the spatially integrated contrast $I_s(t)$ of EBs (eq. [5]) for the EBs' lifetime D, namely,

$$I_{tot} = \int_{t'}^{t'+D} I_s(t')dt' \tag{7}$$

The total integrated contrast is a measure of the total activity of EBs and is, obviously, affected by the recurrence effect.

The analysis hereafter is totally based on parameters obtained under the gaussian correction for unresolved effects.

In Figs. 9a, 9c, 9e, and 9g we provide the differential distribution functions of the duration, the maximum area, the maximum integrated contrast and the total integrated contrast of EBs, respectively, using $I_{c_0} = 0.05$ as the background contrast.

The central feature of the distribution functions of Fig. 9 is their power-law shape. Power laws are

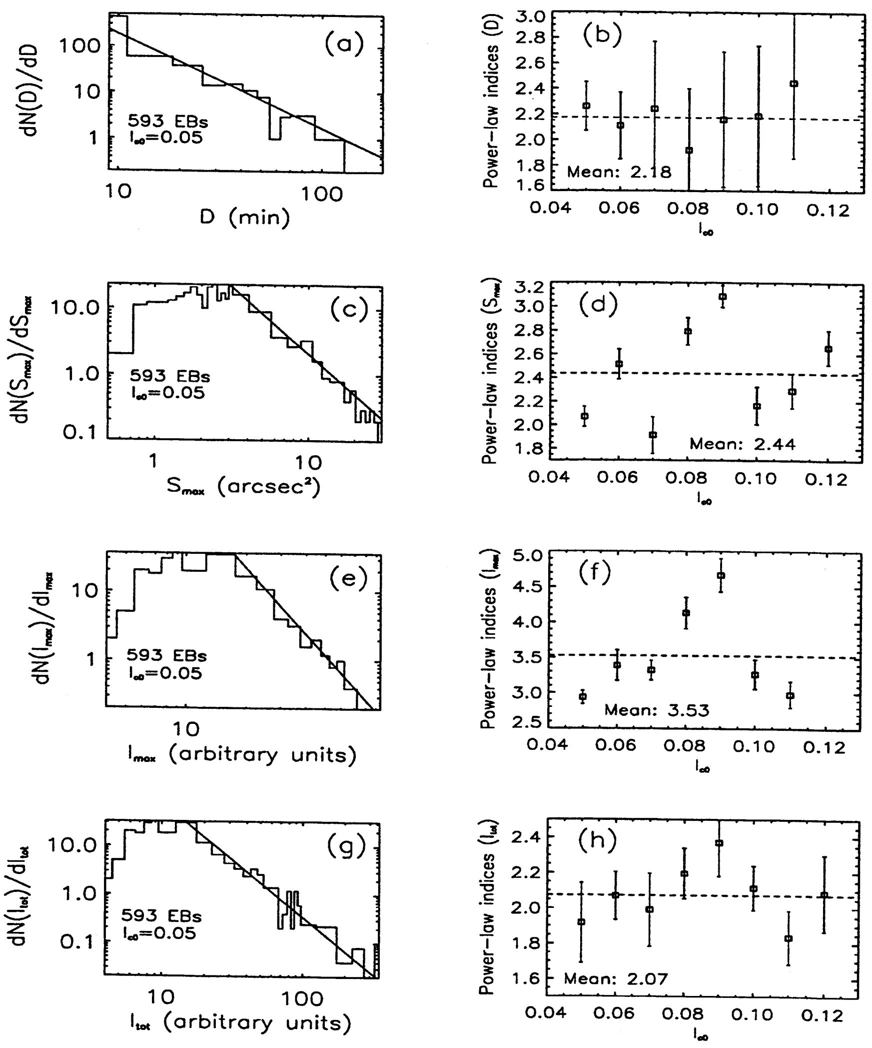

Fig. 9.— Distribution functions and power-law index variations for typical EB parameters: Duration distribution (a) and duration-index variation (b), maximum area distribution (c) and index variation (d), maximum integrated contrast distribution (e) and index variation (f), and total integrated contrast distribution (g) and index variation (h). The best least-squares power-law fits are shown by straight lines (left column). Error bars (right column) show the standard deviation calculated for each index. The mean value of the calculated power-law indices is shown by dashed straight lines (right column).

suggestive of the existence of an intrinsic self-similarity in the triggering process of EBs. Self-similarity, or scale-invariance, in the distribution functions of EB parameters fits well with the fractal properties of EB clustering. This core property of EBs suggests that the same behavior should be expected for undetected EBs, as well, down to the elementary EB sizes. Power laws in Fig. 9 are of the form

$$\frac{dN(X)}{dX} \propto X^{-\alpha_X} \qquad (8)$$

where $X \equiv \{D, S_{max}, I_{max}, I_{tot}\}$ and α_X is the respective power-law index. We obtain power laws for all typical EB parameters, independently of the background selection, provided that the EB

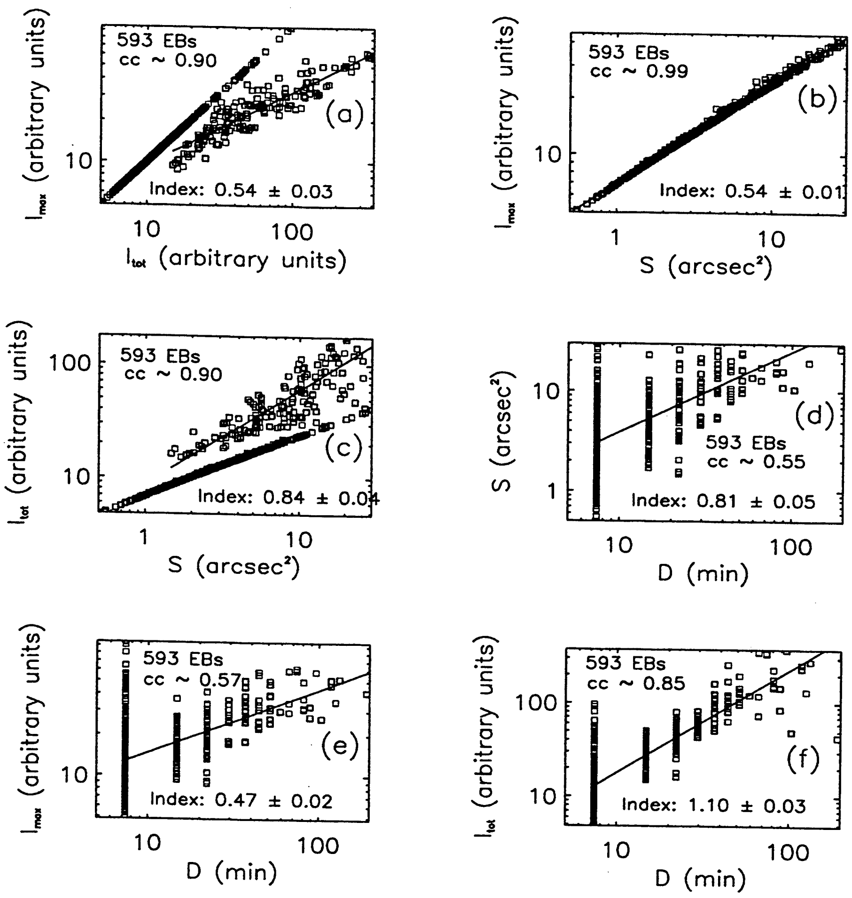

Fig. 10.— Correlation scatter plots linking typical EB parameters for $I_{c_0} = 0.05$. The straight lines correspond to the least-squares power-law best fit. The scatter plots correlate the maximum integrated contrast and the total integrated contrast (a), the maximum integrated contrast and the maximum area (b), the total integrated contrast and the maximum area (c), the maximum area and the duration (d), the maximum integrated contrast and the duration (e), and the total integrated contrast and the duration (f). The straight-line components seen in plots (a) and (c) correspond to EBs with lifetime equal to 1 (frame), for which $I_{tot} = I_{max}$. These events have been excluded from the fitting process. The quality of the correlations is measured by means of the linear correlation coefficient (cc).

numbers are sufficient. In Figs. 9b, 9d, 9f, and 9h we show the variations of the power-law indices a_X for the distribution functions of Figs. 9a, 9c, 9e and 9g, respectively, for different backgrounds I_{c_0}. The error bars in the calculation of the power-law indices become larger as the background increases, since the EB sample becomes smaller and smaller.

We stated previously that we will not pursue conclusions based on the EB duration, because of our moderate cadence. Indeed, from Fig. 9a one notices durations well above 100 *min*, which clearly suggest that the duration distribution function is severely affected by the recurrence effect. Similar EB durations have been obtained in early, low-cadence studies (Bruzek 1972; Vorpahl and Pope 1972).

Although power laws themselves should be viewed as the main result of Fig. 9, it is noteworthy to discuss briefly the values of the power-law indices. We made tests without applying the gaussian correction and we obtained significantly flatter power laws compared to their respective ones in Fig. 9. The correction, therefore, did not change the power-law shape of the distribution functions, but it resulted in different power-law indices. It should be expected that different adopted assumptions give different power laws in all distribution functions, except the duration distribution function which is not subject to any correction. The mean power-law index $\bar{\alpha_D}$ for EB durations is $\bar{\alpha_D} \simeq 2.20$. The mean power-law indices for the maximum integrated contrast and the total integrated contrast are $\bar{\alpha_{I_m}} \simeq 3.53$ and $\bar{\alpha_{I_t}} \simeq 2.07$, respectively. The mean power-law index $\bar{\alpha_S}$ of the EB areas is $\bar{\alpha_S} \simeq 2.44$.

We have, furthermore, investigated possible correlations between typical EB parameters. To achieve this, we have constructed correlation scatter plots linking these parameters. These scatter plots are shown in Fig. 10. Again, we obtain power-law relations between EB parameters, of the form

$$X \propto Y^{\delta_{XY}} \tag{9}$$

where $X, Y \equiv \{D, S_{max}, I_{max}, I_{tot}\}$ and δ_{XY} is the correlation index between parameters X and Y ($\delta_{XY} \equiv 1$ for $X = cY$; c constant). The (linear) correlation coefficients are moderate-to-high, varying in the range (0.55, 0.99). Notice the excellent relation between maximum EB areas and maximum integrated contrasts (Fig. 10b). A high correlation coefficient should be expected, since the maximum integrated contrast of an EB, in most cases, occurs when the EB area peaks. This striking correlation, however, points to an invariant relation between the area and the integrated contrast of EBs, independently of the background selection. This result is not due to the gaussian correction; it is also obtained when the correction is not applied.

The above is the first statistical study of several EB parameters. The power-law distribution functions and the interrelated event parameters, however, are well documented results in the statistical studies of flares, soft X-ray, and extreme ultraviolet (EUV) BPs. Remarkably, the quality of the correlations is even better for EBs, in some cases. We will discuss this result in § 8.

6. Energetics of EBs

We will now estimate typical EB energies. Energy losses in the EB volume, as well as motions associated with EBs, will serve as proxies of the actual released energies. Our results will be compared to previous estimations of EB energies, which vary in the range $(10^{25}, 10^{27})$ erg (Bruzek 1972; Hu, Song, & Li 1995; Hénoux, Fang, & Ding 1998).

Energy losses during EBs should be attributed to radiation and thermal conduction. The conductive losses may be neglected in the low chromosphere, because of the small temperature gradients (Payne 1993). Therefore, the dominant energy loss mechanism in EBs is radiative cooling. We adopt the expression of Nagai (1980) for the net radiative loss rate per unit volume ε_{rad} ($erg\ cm^{-3}\ s^{-1}$), namely,

$$\varepsilon_{rad} \simeq a(T) n^2 \chi g(T) \tag{10}$$

where $a(T)$ is the radiative reduction coefficient, $n = n_e + n_H \simeq n_e$, with n_e, n_H the numerical densities of electrons and neutral hydrogen, respectively, χ is the ionization degree and $g(T)$ is a semi-empirical function of the temperature T. Adopting Nagai's (1980) findings, we obtain $g(T) \simeq 10^{-23} erg\ cm^3\ s^{-1}$, for $T = 10^4\ K$, assuming that this temperature is typical of the EB volume. For $T \leq 5 \times 10^4\ K$, moreover, the ionization degree is approximated by the expression (Brown 1973)

$$log \frac{\chi^2}{1-\chi} = -log n - \frac{51405}{T} + 0.5 log T + 16.0039 \tag{11}$$

Payne (1993) used a numerical density $n \simeq n_e \simeq 2.24 \times 10^{12} cm^{-3}$ in the EB volume. This density is consistent with works on radiative transfer models (Canfield and Gayley 1987; Hawley and Fisher 1994; Abbett and Hawley 1999) of solar flare atmospheres. These models predict a broadening of the $H\alpha$ line, similar to that obtained in EBs, when a sharp temperature increase ($\Delta T \sim 10^3 - 10^4\ K$) occurs, followed by an abrupt increase of the ionization degree. The high ionization degree allows plasma confinement due to the fact that the magnetic field is stronger than the equipartition value and the density is kept in the range $(10^{12}, 10^{13})$ cm^{-3}. Adopting $n \simeq 10^{12} cm^{-3}$ and $T = 10^4\ K$ in EBs, we obtain, from equation

(11), $\chi \simeq 0.89$. Moreover, we obtain (Nagai 1980) $a(T) \simeq 0.1$ for $T \simeq 10^4\ K$. Therefore, we find from equation (10) that the net radiative loss rate in EBs is $\varepsilon_{rad} \simeq 0.89\ erg\ cm^{-3}\ s^{-1}$.

Knowledge of the EB radiative volume and the EB duration are required to calculate the peak and the total radiative losses during EBs. The EB volume V_{EB} may be approximated by the relation $V_{EB} \sim Sh$, where S is the area occupied by an EB and h is the vertical extent (height) of EBs. We have established the association of EBs with 1600 Å BPs in the T_{min} region which allows a conservative estimate of the EB height, that is, $h \simeq 10^2\ km$. Other authors (Kitai and Muller 1984) argue that even a height $h \sim 10^3\ km$ should not be ruled out.

The peak radiative loss rate (peak luminosity) P_{rad} ($erg\ s^{-1}$) of EBs is given by the relation

$$P_{rad} = \varepsilon_{rad} f V_{EB(max)} \qquad (12)$$

where $V_{EB(max)} \sim S_{max} h$ is the maximum volume attained by a given EB. This volume is assumed linearly related to the maximum area S_{max}, calculated for this EB, and a typical height $h = 10^2\ km$. f is the radiative filling factor, which is considered unity, thus assuming that the entire EB volume radiates during the energy release process. To calculate the total radiative losses E_{rad} over the EBs' lifetime, we further need to adopt a typical temporal profile of EBs: EBs are assumed either symmetric with a plateau roughly equal to the peak released energy (Payne 1993) or symmetric with roughly equal rise and decay times (Qiu et al. 2000). We adopt the second assumption, thus obtaining

$$E_{rad} \sim \frac{P_{rad} D}{2} \qquad (13)$$

where D is the lifetime of an EB showing a peak luminosity equal to P_{rad}. The first assumption provides a larger E_{rad}, by a factor of two. Although we have roughly estimated the durations of EBs in our sample, we underlined that our estimations should not be considered reliable, due to the moderate cadence, compared to typical EB lifetimes, and the recurrence effect. Indeed, the latter effect is obvious in Fig. 9a. Therefore, we will use typical EB lifetimes, provided by previous authors. The adopted typical value of EB lifetimes is $D_{EB} \simeq 600\ s$ (10 min). We have, moreover, applied the correction for unresolved effects to the calculation of the maximum EB areas S_{max}.

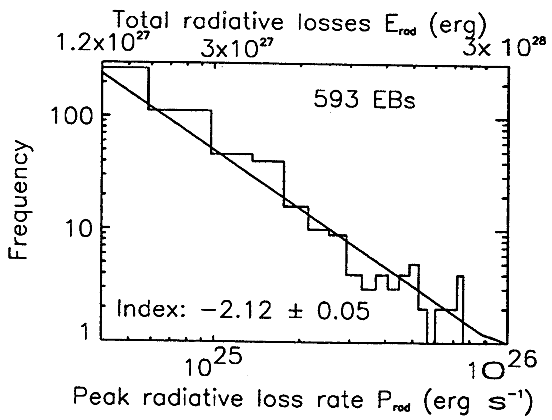

Fig. 11.— Differential distribution function of the peak and the total radiative losses in EBs for a background contrast $I_{c_0} = 0.05$. Calculations have been performed assuming a vertical extent of the EB volume equal to 100 km, an EB duration equal to 10 min and a temperature of the radiative volume equal to $10^4\ K$. The straight line is the least-squares power-law best fit.

The differential distribution functions of the peak and the total radiative losses in EBs are given in Fig. 11 for $I_{c_0} = 0.05$. The peak radiative losses in EBs vary in the range $(4 \times 10^{24}, 10^{26})\ erg\ s^{-1}$, while the total energy losses due to radiative cooling of EBs vary between $\sim 1.2 \times 10^{27} erg$ and $\sim 3 \times 10^{28} erg$. Another notable feature in Fig. 11 is the power-law shape of the distribution function. The (peak and total) radiative energy losses E of EBs obey a distribution function $\frac{dN(E)}{dE} \propto E^{-\alpha}$, with power-law index $\alpha = 2.12 \pm 0.05$. It should be noted that the power law obtained in Fig. 11 depends largely on the power law of the maximum EB areas (Fig. 9c) and, therefore, on the gaussian correction. Moreover, it depends on the fact that we adopt a constant, typical EB lifetime. Conclusions relying on the value of the power-law index should be considered with care.

On the other hand, EBs are often associated with kinematic events. Rust (1968) reported the correlation of EBs with surges, ejecting with velocities $\sim 10^2\ km\ s^{-1}$ and showing threads $\sim 5 \times 10^3\ km$ high. Assuming a thread-like surge with a height $\sim 5 \times 10^8\ cm$, an aspect ratio of, say, 10, that is, a diameter of $\sim 5 \times 10^7$ *cm* (500 *km*), an electron density $\sim 10^{11} cm^{-3}$ and a velocity $\sim 10^7$ $cm\ s^{-1}$, then the kinetic energy of the surge is $\sim 4.5 \times 10^{26} erg$. The radiative energy of the surge is $\sim 10^{26} erg$, thus giving a total surge energy $\sim 5.5 \times 10^{26} erg$. Although the association of EBs with surges is not clear in this work, we find that a total surge energy of $\sim 5.5 \times 10^{26} erg$ is comparable to the total radiative losses in EBs, at least in case of the weaker events. If the released energy during EBs triggers surges then, based on our calculations, the total radiative losses and kinematic effects are balanced by a total released energy in the range $(1.8 \times 10^{27}, 3 \times 10^{28})$ *erg*. This estimation is, in general, consistent with the previously reported energy range of EBs, although it is somewhat shifted toward higher energies.

If the numerical density in the EB volume is of the order $10^{12} cm^{-3}$, what is the temperature enhancement in EBs ? For the net radiative energy loss rate ε_{rad} to be balanced by a thermal energy input, we require a temperature enhancement ΔT, given by the relation

$$\varepsilon_{rad} \simeq \frac{3}{2} n k_B \Delta T \qquad or \qquad \Delta T \simeq \frac{2\varepsilon_{rad}}{3 n k_B} \qquad (14)$$

where $n \simeq n_e + n_i \simeq 2 \times 10^{12} cm^{-3}$ and k_B is the Boltzmann constant. For $\varepsilon_{rad} = 0.89\ erg\ cm^{-3} s^{-1}$, we obtain, from equation (14), $\Delta T \simeq 2.15 \times 10^3\ K$. This temperature enhancement is not beyond reason and, in fact, it is close to the temperature enhancement of $\sim 1.5 \times 10^3\ K$, suggested by Kitai (1983). To account for both radiative losses and mass motions in surges, a well-defined EB with $S_{max} \sim 10\ arcsec^2$ and duration $D \sim 10\ min$ requires a temperature enhancement $\Delta T \simeq 4.3 \times 10^3\ K$. In the above analysis, we have implicitly neglected the possibility of a non-thermal energy release component which may, as well, be present during EBs. Based on our thermal calculations, the rate of energy release, for a reasonable $\Delta T \simeq 2.15 \times 10^3\ K$, is comparable to the radiative cooling rate. The cooling timescale responding to a single energy deposition, therefore, should be short, of the order of a few *s*. This result is consistent with the results of non-LTE radiative transfer models (Abbett and Hawley 1999) that predict short cooling timescales in heated plasmas in the chromosphere, characterized by a line broadening in $H\alpha$.

7. An interpretation of EB triggering

Our results (§ 4) suggest that EBs occur on the interface of colliding magnetic configurations, either above or in the absence of photospheric magnetic neutral lines. An intriguing feature of such complex topologies is the likely presence of quasi-separatrix layers (QSLs - van Driel Gesztelyi et al. 1994; Démoulin et al. 1996; Démoulin et al. 1997). QSLs are a generalization of separatrices, which apply to magnetic null points, to three-dimensional configurations which do not necessarily require nulls (Démoulin and Priest 1997). QSLs, or separatrices, are formed on the interface between different flux systems, that is, where the magnetic connectivity pattern changes. It is expected, therefore, that separatrices and QSLs are formed *(i)* on the dipolar supergranular boundaries, *(ii)* on MDFs, and *(iii)* between emerging vertical fields and pre-existing horizontal fields at the vicinity of the leading spot, since the two topologies are geometrically different. The above areas are all prolific in EB production. It is likely, therefore, that EBs occur on separatrices and QSLs in the low chromosphere.

In Fig. 12 we show schematically how our data support this triggering cause for EBs. In Fig. 12a we show a magnetic configuration similar to the one expected for the supergranular boundaries. The strong neutral lines are sustained by converging flows and an X-point separatrix forms between the two flux systems. The EB occurs on the separatrix, above the photospheric neutral line. In Fig. 12b, small X-point separatrices are formed above MDFs. The MDF configurations in both our data and Fig. 12b appear inclined toward the direction of the flow. The EBs occur above the neutral lines of the MDFs. Our MDFs exhibit a U-loop shape, instead of the classical, emerging, Ω-loops (Bernasconi et al. 2002). The absence of apparent links (magnetic field lines) with higher atmospheric layers probably explains the lack of correlations between EBs above MDFs and 1600 Å BPs, pointed out in § 4.3. In Fig. 12c, a QSL is formed between the pre-existing, nearly horizontal magnetic field and the relatively perpendicular moving magnetic flux bundles. In our data, this is shown by the gradient of the zenith angle between the two configurations in area 3 (Fig. 7). The EB of Fig. 12c occurs in the unipolar area of the interacting, topologically different magnetic structures. Our results regarding the magnetic field topology in area 3 are consistent with the results of Lites, Skumanich, & Martinez Pillet (1998). The relatively horizontal fields form the low-lying magnetic canopy with weak magnetic fields, that connects the two sunspots. The relatively vertical fields are the newly emerged individual flux elements that attain significant horizontal velocities and strong, vertical magnetic fields when they migrate away from the flux emergence zone. In all shown scenarios of EB triggering, in Fig. 12, EBs occur close to the photospheric footpoints of magnetic field lines. This probably explains the downflows associated with almost all EBs, as being drainage motions of previously elevated, cold material, toward the photospheric footpoints of emerged flux ropes (Bruzek 1967; Zwaan 1985).

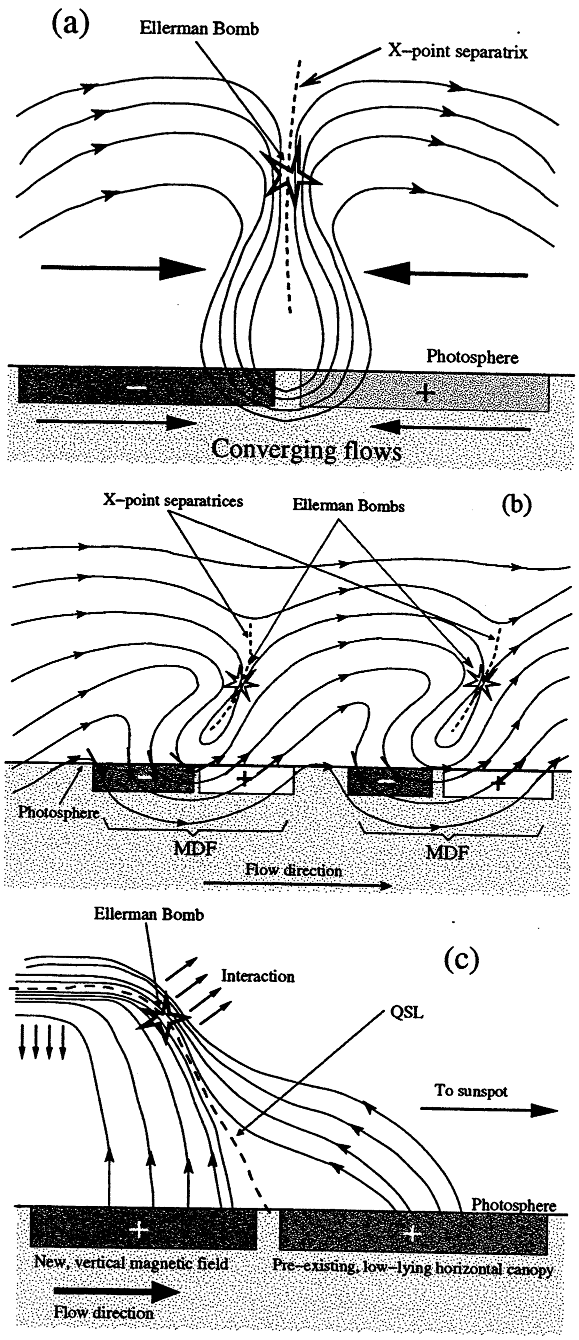

Fig. 12.— Three different mechanisms of EB triggering on separatrices and QSLs. (a) Magnetic reconnection in strong, dipolar magnetic fields sustained by converging horizontal flows. (b) EBs triggered by magnetic reconnection above MDFs. (c) EB triggered by the interaction of two topologically different, unipolar, magnetic configurations.

Separatrices and QSLs (hereafter QSLs, for brevity) are candidate areas for magnetic reconnection on the photosphere/low chromosphere. In fact, they may be the only locations in the lower atmosphere that allow a large growth rate of the tearing mode instability, especially at the vicinity of the T_{min} region (Sturrock 1999). Magnetic reconnection normally requires current sheets formed by anti-parallel magnetic fields but we obtain EBs in both dipolar and unipolar areas. However, in both theory (Soward 1982) and numerical simulations (Linton, Dahlburg, & Antiochos 2001), it has been reported that reconnection can be efficient even at small contact angles between the interacting magnetic field lines. Free magnetic energy is accumulated on QSLs. Stochastic magnetic reconnection in a turbulent environment effectively releases the free energy and fragments QSLs. Our data favor EB triggering by magnetic reconnection on QSLs, due to the turbulent evolution of the magnetic field. This process probably accounts for *(i)* the self-similarity in EB statistics, *(ii)* the small sizes of EBs, and *(iii)* the preferred elongated EB shape, reminiscent of a Petschek reconnection scenario.

8. Summary and Discussion

EBs occur in areas of strong, colliding magnetic configurations. In particular, they occur:

(1) Above magnetic neutral lines outlining the boundaries of supergranular cells.

(2) Above the magnetic neutral lines of MDFs.

(3) In the absence of neutral lines, when topologically different magnetic configurations interact. In this case, EBs are triggered due to the interaction between the pre-existing, low-lying horizontal magnetic canopy and plage-like, strong vertical fields, at the vicinity of the leading sunspot.

The above locations are most prominent in EB triggering throughout our entire observing time, thus resulting in an inhomogeneous spatial distribution of EBs. EBs appear in clusters, or swarms, in these preferential locations. The recurrence effect of EBs originates from this behavior.

The correlation of EBs with photospheric mass flows is as follows:

(1) The Doppler photospheric velocities beneath EBs indicate downflows. In several cases, EBs occur above the edge of areas dominated by downflows. We have seen EBs associated with upflows but, in these cases, there is a relative downflow in the locations of EBs, with respect to the EBs' surroundings. Downflows probably occur due to drainage motions of cold material toward the photospheric footpoints of previously emerged flux ropes.

(2) EB loci move parallel to transverse photospheric flows, as calculated by correlation-tracking techniques applied on the FGE white-light images. This behavior is clearly seen in areas of systematic transverse flows, such as the supergranular area and the vicinity of the leading sunspot. On the boundaries of the supergranule, which are sustained by converging transverse flows, EB loci move with smaller velocities.

The typical EB size is 1.8×1.1 *arcsec*^{2}. EBs exhibit an elongated shape with their length 40% larger than their width. A large number of EBs have sizes close to, or even below, our spatial resolution (0.8 *arcsec*). This suggests that improved spatial resolution may set the typical EB sizes to even lower values. We found a mean EB occurrence rate ~ 1.43 EBs min^{-1} for an EB-producing area ~ 1800 *arcsec*^{2}. Given our moderate cadence (7.5 *min*), the recurrence effect, our finite spatial resolution, and the overlaying AFS filaments which may obscure several EBs, we conclude that this occurrence rate is only a lower limit of the actual occurrence rate of EBs.

The spatial distribution of EBs is not only inhomogeneous; in several cases one may calculate reliably a fractal dimension of the EB clusters. The fractal behavior of EB clustering occurs for any given background definition, provided that the statistics are sufficient. Although different definitions of the background give rise to different estimations of the fractal dimension, the value of the fractal dimension does not change significantly in the course of time for a given background. For a background contrast $I_{co} = 0.08$, the mean fractal dimension of EB clusters is ~ 1.4. The relative constancy of the fractal dimension suggests that the clustering preferences of EBs do not change during our observing interval. This is because the prolific areas in EB production (the supergranular boundaries and the vicinity of the leading spot), or the flux emergence process in general, have lifetimes longer than our observing time (~ 3.5 *h*).

We defined and calculated typical parameters of EBs, such as EB areas, maximum and total integrated contrasts. To account for unresolved effects and the finite spatial resolution, we applied a gaussian correction. Independently of the application of this correction, the differential distribution functions of all typical EB parameters exhibit a robust power-law shape. Moreover, all EB parameters are non-linearly interrelated, with correlation diagrams obeying power laws. This result is shown for the first time in an EB study, but it is well documented in studies of explosive events in the EUV and soft X-rays, as well as in studies of hard X-ray flares (Crosby, Aschwanden, & Dennis 1993; Bromund, McTiernan, & Kane 1995; Crosby 1996; Georgoulis, Vilmer, & Crosby 2001).

In terms of energetics, EBs have typical subflaring energies. To account for the calculated radiative losses and kinematic effects, the peak rate of energy release in EBs should vary in the range $(4 \times 10^{24}, 10^{26})$ $erg\ s^{-1}$, with the total released energy in the range $(1.8 \times 10^{27}, 3 \times 10^{28})$ *erg*, assuming a typical EB duration of ~ 10 *min*. We have shown that EBs appear in at least two wavelengths, namely, the wings of the $H\alpha$ line and the 1600 Å continuum, indicating a vertical extent of

at least 100 km. If the bulk of the released energy is thermal, then the EB volume is heated at a temperature $\sim 2 \times 10^3$ K higher than the ambient temperature in the low chromosphere and responds to an instantaneous heat deposition with a cooling timescale of the order of a few s. The distribution function of EB energies obeys a power law with index ~ -2.1. While power laws in the distribution function of EB energies should be expected in any case, the power-law index is sensitive to the assumptions under which energies are estimated (constant EB lifetime and the gaussian correction).

For decades, EBs have been a puzzling aspect of the activity in the low chromosphere. Two questions concerning EBs, namely *(i)* their triggering mechanism and *(ii)* their role on chromospheric dynamics and heating, are still elusive. We have shown (§ 7) that the locations of EB triggering are, quite likely, parts of QSLs in the low chromosphere. Turbulence plays a key role in the evolution of QSLs and the free magnetic energy cascades down to small scales, to be released by stochastic magnetic reconnection. This intrinsic self-similarity fits nicely with the power laws uncovered in every aspect of EB statistics and with the fractal properties of EB clustering. The typical peak EB energies are similar to the energies of the theoretical nanoflares, postulated by Parker (1988). Although dependent on various assumptions, the power-law index of EB energies (~ -2.1) suggests that EBs contribute significantly to the heating of the low chromosphere in the active region. If the power-law index is smaller than -2, then it can be readily shown that the bulk of the integrated energy content of the distribution functions stems from the low-energy part (Hudson 1991). Large numbers of un-detected EBs, therefore, may release substantial amounts of energy. It is very likely that our distribution functions fail to include the weaker EBs, since typical EB sizes are close to our spatial resolution and numerous EBs are hardly detectable. Since EBs occur close to the footpoints of flux ropes, it is likely that they heat significantly the low chromosphere and trigger disturbances that propagate along the field lines, thus contributing to a coronal heating process which originates from low-altitude magnetic reconnection.

The idea that EBs are flare-like events is not new; it was first proposed in early studies by Severny and co-workers (Severny 1968 and references therein). Our work, based on a large, seeing-free EB sample and high-resolution photospheric observations, suggests that magnetic reconnection may indeed be a viable triggering mechanism of EBs. Several statistical properties of EBs are similar to statistical properties of EUV and soft X-ray BPs in the transition region and the low corona (Shimizu 1995; Krucker & Benz 1998; Berghmans, Clette, & Moses 1998; Parnell & Jupp 2000; Aschwanden et al. 2000; Aletti et al. 2000). Several of our conclusions, therefore, could be proved valid for these transients, higher in the atmosphere.

EBs are familiar to experienced solar observers but their significance and impact in various aspects of chromospheric dynamics has probably been overlooked. A significant effort needs to be focused on the study of EBs. Attempts to interpret EBs by means of phenomenological, or MHD/radiative transfer, models, are highly desired. If it is shown that EBs are signatures of low-altitude reconnection and a viable means of chromospheric heating, this would be an important advance. Such a result would explain why emerging flux regions, typically showing swarms of EBs, appear brighter than fully developed ARs, with far fewer EBs and a decaying magnetic evolution.

We are grateful to Dr. B. J. LaBonte who contributed to the calibration of the magnetograms and the Dopplergrams and provided numerous comments and advice, to Dr. R. A. Shine who provided us with the results of the correlation-tracking technique, and to H. A. C. Eaton who reduced and co-aligned the white-light images and contributed to the calibration of the $H\alpha$ filtergrams. We are also grateful to the TRACE mission science team for making their images available, and for coordinating TRACE observations during the flight of the Flare Genesis Experiment. We thank Prof. L. Vlahos and Drs. A. Nindos and S. Patsourakos for a critical reading, as well as for their prompt comments on the manuscript. This work has received support from NASA grant NAG5-8331, NSF grant OPP-9909167 and earlier NASA Solar Physics Program and NSF Polar Program grants for development and flight of the Flare Genesis Experiment.

A. Gaussian correction for finite spatial resolution and unresolved effects in EBs

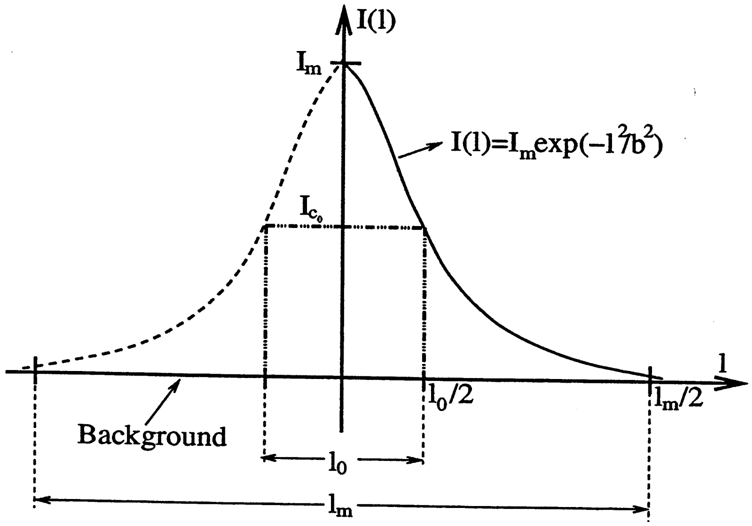

Fig. 13.— Application of the gaussian correction for an EB at a given time (frame): The EB contrast faints accordingly away from the pixel with the maximum contrast at that time. For a background contrast $I(l) = I_{c_0}$ we measure an EB area S_0, which results in a length l_0, calculated under the assumption of an elliptical EB shape with the length 40% larger than the width. The corrected EB length is l_m, from which we calculate the corrected EB area S_m.

Let us assume that the contrast $I(l)$ of an EB at any given frame faints as a gaussian function of the distance l from the pixel of maximum contrast I_m, that is,

$$I(l) = I_m exp[-\frac{l^2}{b^2}] \tag{A1}$$

with b being the width of the gaussian (Fig. 13).

For a background contrast I_{c_0} we measure an EB surface S_0, that is, an EB length $l_0 \simeq 1.3(S_0/\pi)^{1/2}$, assuming that the EB exhibits an elliptic shape with a length l_0 40% larger than the width w_0. This assumption is supported by our results (Fig. 3). Equation (A1), therefore, becomes

$$I(S) \simeq I_m exp[-0.54\frac{S}{b^2}] \tag{A2}$$

The corrected length of the EB is $l_m \simeq 1.3(S_m/\pi)^{1/2}$, with S_m being the corrected EB area. Setting the background contrast equal to unity and assuming (Fig. 13) that $I(S) = 1$ for $l = l_m/2 \simeq 0.37S_m^{1/2}$, we obtain

$$b^2 \simeq \frac{0.37S_m}{lnI_m} \tag{A3}$$

Substituting equation (A3) into equation (A2) we obtain

$$I(S) \simeq I_m^{1-1.46(S/S_m)} \tag{A4}$$

Moreover, for $I(S) = I_{c_0}$ we obtain $l = l_0/2$. Substituting this information in equation (A2), one may calculate the corrected area S_m of the EB at a given frame as a function of the measured area S_0 of the

EB at that frame, the peak EB contrast I_m at that frame, and the prescribed background contrast I_{c_0} as follows:

$$S_m = S_0 \frac{log I_m}{log(I_m/I_{c_0})} \tag{A5}$$

The corrected, spatially integrated contrast $I_s(t)$, at a given time t (a given frame), is provided by the integral

$$I_s(t) = 2 \int_0^{l_m/2} I(l)dl \tag{A6}$$

Substituting equation (A1) into equation (A6), we obtain

$$I_s(t) = 2I_m b \int_0^{l_m/2b} e^{-u^2} du \ ; \qquad u = \frac{l}{b} \tag{A7}$$

which transforms to

$$I_s(t) \simeq b I_m \sqrt{\pi}\, erf(\frac{l_m}{2b}) \tag{A8}$$

or, in terms of the corrected area S_m,

$$I_s(t) \simeq b I_m \sqrt{\pi}\, erf(\frac{0.74 S_m^{1/2}}{2b}) \tag{A9}$$

with $erf(x) \equiv \frac{2}{\sqrt{\pi}} \int_0^x e^{-u^2} du$ being the error function of the quantity x. The coefficient b is given by equation (A3).

REFERENCES

Abbett, W. P. & Hawley, S. L., 1999, ApJ, 521, 906

Aletti, V., Velli, M., Bocchialini, K., Einaudi, G., Georgoulis, M., & Vial, J.-C., 2000, ApJ, 544, 550

Aschwanden, M. J., Tarbell, T. D., Nightingale, R. W., Schrijver, C. J., Title, A., Kankelborg, C. C., Martens, P., & Warren, H. P., 2000, ApJ, 535, 1047

Berghmans, D., Clette, F. & Moses, D., 1998, A&A, 336, 1039

Bernasconi, P. N., Rust, D. M., Eaton, H. A. C., & Murphy, G. A., 2000, in Air-borne Telescope Systems (eds.: Melugin, R. K., & Röser, H. P.), Proc. SPIE, 4014, 214

Bernasconi, P. N., Rust, D. M., & Eaton, H. A. C., 2001, ASP Conference Series, 236, 399

Bernasconi, P. N., Rust, D. M., Georgoulis, M. K., & LaBonte, B. J., 2002, SoPh, submitted

Bromund, K. R., McTiernan, J. M., & Kane, S. R., 1995, ApJ, 455, 733

Brown, J. C., 1973, SoPh, 39, 421

Bruzek, A., 1967, SoPh, 2, 451

Bruzek, A., 1972, SoPh, 26, 94

Canfield, R. C. & Gayley, K. G., 1987, ApJ, 322, 999

Crosby, N. B., Aschwanden, M. J., & Dennis, B. R., 1993, SoPh, 143, 275

Crosby, N. B., 1996, Ph. D. Thesis, Université de Paris VII, Paris, France

Dara, H. C., Alissandrakis, C. E, Zachariadis, Th. G., & Georgakilas, A. A., 1997, A&A, 322, 653

Démoulin, P., Bagala, L. G., Mandrini, C. H., Hénoux, J. C., & Rovira, M. G., 1997, A&A, 325, 305

Démoulin, P., Hénoux, J. C., Priest, E. R., & Mandrini, C. H., 1996, A&A, 308, 643

Démoulin. P. & Priest, E. R., 1997, SoPh, 175, 123

Denker, C., 1997, A&A, 323, 599

Ding, M. D., Hénoux, J.-C., & Fang, C., 1998, A&A, 332, 761

Diver, D. A., Brown, J. C., & Rust, D. M., 1996, SoPh, 168, 105

van Driel-Gesztelyi, L. & Petrovay, K., 1990, SoPh, 126, 285

van Driel-Gesztelyi, L., Hofmann, A., Démoulin, P., Schmieder, B., & Csepura, G., 1994, SoPh, 149, 309

Ellerman, F., 1917, ApJ, 46, 298

Engvold, O. & Maltby, P., 1968, in Mass Motions in Solar Flares and Related Phenomena (ed.: Ohman, Y.), Nobel Symp. 9, 109

Fan, Y., Fisher, G. H., & DeLuca, E. E., 1993, ApJ, 405, 390

Georgoulis, M. K., Vilmer, N., & Crosby, N. B., 2001, A&A, 367, 326

Hawley, S. L. & Fisher, G. H., 1994, ApJ, 426, 387

Hénoux, J.-C., Fang, C., & Ding, M. D., 1998, A&A, 337, 294

Hu, F. M., Song, M. T., & Li, X. Q., 1995, ApSS, 229, 325

Hudson, H. S., 1991, SoPh, 133, 357

Ji, H. S., Song, M. T., & Li, X. Q., 2001, SoPh, 198, 133

Kitai, R., 1983, SoPh, 87, 135

Kitai, R. & Muller, R., 1984, SoPh, 90, 303

Koval, A. N. & Severny, A. B., 1970, SoPh, 11, 276

Krucker, S. & Benz, A. O., 1998, ApJ, 501, L213

Kurokawa, H., Kawaguchi, I., Funakoshi, Y., & Nakai, Y., 1982, SoPh, 79, 77

Linton, M. G., Dahlburg, R. B., & Antiochos, S. K., 2001, ApJ, 553, 905

Lites, B. W., Skumanich, A., & Martinez Pillet, V., 1998, A&A, 333, 1053

Mandelbrot, B., 1983, The Fractal Geometry of Nature, New York: Freeman

McMath, R. R., Mohler, O. C., & Dodson, H. W., 1960, Proc. Nat. Acad. Sci., U.S., 46, 165

Nagai, F., 1980, SoPh, 68, 351

Nindos, A. & Zirin, H., 1998, SoPh, 182, 381

Parker, E. N., 1988, ApJ, 330, 474

Parnell, C. E. & Jupp, P. E., 2000, ApJ, 529, 554

Payne, T., 1993, PhD Thesis, New Mexico State University, New Mexico, USA

Petrovay, K., Brown, J. C., van Driel-Gesztelyi, L., Fletcher, L., Marik, M., & Stewart, G., 1990, SoPh, 127, 51

Pikel'ner, S. B., 1974, Astron. Zh., 51, 233

Qiu, J., Ding, M. D., Wang, H., Denker, C., & Goode, P. R., 2000, ApJ, 544, L157

Ronan, R. S., Mickey, D. L., & Orrall, F. Q., 1987, SoPh, 113, 353

Roy, J.-R. & Leparskas, H., 1973, SoPh, 30, 449

Rust, D. M., 1968, in Structure and Development of Solar Active Regions (ed.: Kiepenheuer, K. O.), IAU Symp. No 35, 77

Rust, D. M., 1994a, Adv.Sp.Res., 14, 89

Rust, D. M., 1994b, Optical Eng., 33, 3342

Severny, A. B., 1964, ARA&A, 2, 363

Severny, A. B., 1965, SvA, 9, 171

Severny, A. B., 1968, in Mass Motions in Solar Flares and Related Phenomena (ed.: Ohman, Y.), Nobel Symp. 9., 71

Shimizu, T., 1995, PASJ, 47, 251

Soward, A. M., 1982, J. Plasma Phys., 28, 415

Stellmacher, G. & Wiehr, E., 1991, A&A, 251, 675

Sturrock, P. A., 1999, ApJ, 521, 451

Vernazza, J. E., Avrett, E. H., & Loser, R., 1981, ApJSS, 45, 635

Vorpahl, J. & Pope, T., 1972, SoPh, 25, 347

Wilson, P. R., 1981, SoPh, 69, 9

Zachariadis, Th. G., Alissandrakis, C. E., & Banos, G., 1987, SoPh, 108, 227

Zwaan, C., 1985, SoPh, 100, 397

This 2-column preprint was prepared with the AAS LaTeX macros v5.0.

FINAL REPORT, Grant NAG5-8331

Flare Genesis Experiment
D. M. Rust, Principal Investigator
The Johns Hopkins University Applied Physics Laboratory

Report period: May 1999 – April 2002

The work accomplished under the subject grant is described in the following publications and presentations. Two articles that are now in press are appended to describe the very latest scientific findings.

Publications

Bernasconi, P. N., D. M. Rust, G. Murphy, and H. A. C. Eaton, High Resolution Polarimetry with a Balloon-borne Telescope: The Flare Genesis Experiment, in High Resolution Solar Physics: Theory, Observations and Techniques, T. R. Rimmele, K. S. Balasubramaniam, and R R. Radick (eds.), Astron. Soc. Pacific Conf. Series Vol. 183, pp. 279 - 287, 1999.

Bernasconi, P. N., D. M. Rust, H. A. C. Eaton, and G. Murphy, A Balloon-borne Telescope for High Resolution Imaging and Polarimetry, in Airborne Telescope Systems, Proc. SPIE, 4014, R. K. Melugin and H. P. Roeser (eds.), pp. 214-225, 2000.

Rust, D. M., Solar Filaments as Tracers of Subsurface Processes, J. Astrophys. Astron. (India), 21, 177-186, 2000.

Rust, D. M., Solar Prominences, in Encyclopedia of Astronomy and Astrophysics P. Murdin (Ed.), Institute of Physics Pub., Bristol, 2001, p. 2710.

Rust, D. M., Solar Chromosphere: Ellerman Bombs, in Encyclopedia of Astronomy and Astrophysics P. Murdin (Ed.), Institute of Physics Pub., Bristol, 2001, p. 2482.

Rust, D. M., A New Paradigm for Solar Filament Eruptions, J. Geophys. Res. 106 , p. 25,075, 2001.

Bernasconi, P. N., D. M. Rust, and H. A. C. Eaton, High Resolution Vector Magnetograms with the Flare Genesis Vector Polarimeter, in M. Sigwarth (ed.), Advanced Solar Polarimetry – Theory, Observation, and Instrumentation, ASP Conf. Ser. 236, 2002, p. 399-406.

Georgoulis, M. K., D. M. Rust, P. N. Bernasconi, and B. Schmieder, Statistics, Morphology, and Energetics of Ellerman Bombs, Astrophys. J. (in press), 2002.

Bernasconi, P. N., D. M. Rust, M. K. Georgoulis, and B. J. LaBonte, Moving Dipolar Features in an Emerging Flux Region, Solar Phys. (in press), 2002.

Presentations

Eaton, H., Bernasconi, P., Strohbehn, K., and Rust, D. M., An Image Motion Compensation System for the Flare Genesis Balloon-Borne Solar Telescope, JHU/APL Research and Development Symposium, Laurel, MD, November 2 - 3, 1999.

Rust, D. M., Looking at the Sun from 20 Miles above McMurdo, Sunday Science Presentation, McMurdo Base, Antarctica, December 5, 1999.

Rust, D. M., The Necessity of Filament Eruptions, International Conference on Solar Eruptive Events, Washington, DC, March 6 – 9, 2000.

Bernsconi, P., Rust, D. M., Eaton, H. A., and Murphy, G. A., Balloon-Borne Telescope for High-Resolution Solar Imaging and Polarimetry, SPIE Intl. Symposium on Astronomical Telescopes and Instrumentation 2000, Munich, Germany, Mar 28, 2000.

Bernasconi, P., Rust, D. M., Eaton, H. A., and Murphy, G. A., First Results from the January 2000 Flare Genesis Flight, Amer. Geophysical Union Spring Meeting, Washington, DC, May 30 – June 3, 2000.

Rust, D. M., Bernasconi, P. N., Eaton, H. A., Keller, C., Murphy, G. A. and Schmieder, B., New Results from the Flare Genesis Experiment, Solar Physics Division of the Amer. Astron. Soc., Lake Tahoe, CA, June 18 – 22, 2000.

Bernasconi, P. N., Rust, D. M., Eaton, H. A., and Murphy, G. A., Design and Performance of the Flare Genesis Experiment, Solar Physics Division of the Amer. Astron. Soc., Lake Tahoe, CA, June 18 – 22, 2000.

Bernasconi, P. N., D. M. Rust, and H. A. C. Eaton, High Resolution Vector Magnetograms with the Flare Genesis Vector Polarimeter, Sacramento Peak Summer Workshop on Advanced Solar Polarimetry – Theory, Observation, and Instrumentation, Sunspot, NM, September 15 – 19, 2000.

Rust, D. M., Solar Astronomy from 25 Miles Above Antarctica, guest lecture at National Capitol Astronomers Meeting, Bethesda, MD, February 3, 2001.

Rust, D. M., Bernasconi, P. N., Georgoulis, M. K., Shine, R. A. and Schmieder, B., Emerging Flux as seen with the Flare Genesis Experiment, Science Definition Workshop on High-Resolution Solar Magnetography from Space, Natl. Space Sci. Tech. Ctr., Univ. Alabama, Huntsville, AL, April 3, 2001.

Georgoulis, M. K., Rust, D. M., Bernasconi, P. N., Ellerman Bombs in a Solar Active Region: Statistical Properties and Implications, Amer. Geophysical Union Spring Meeting, Boston, MA, May 28 – June 2, 2001.

Rust, D. M., Bernasconi, P. N., Georgoulis, M. K., LaBonte, B. J., Schmieder, B., Sunspot Formation from Emerging Flux Ropes - Observations from Flare Genesis, Amer. Geophysical Union Spring Meeting, Boston, MA, May 28 – June 2, 2001.

Bernasconi, P. N., Rust, D. M., Georgoulis, M. K., LaBonte, B. J., Schmieder, B., Peculiar Moving Magnetic Features Observed With the Flare Genesis Experiment, Amer. Geophysical Union Spring Meeting, Boston, MA, May 28 – June 2, 2001.

Rust, D. M., Bernasconi P. N., Georgoulis M. K., LaBonte B. J., Schmieder, B., Activity in Emerging Flux Region NOAA 8844, Observational Challenges for the Next Decade of Solar Magnetohydrodynamics, Institute for Theoretical Physics, Santa Barbara, CA, January 17, 2002.

Rust, D. M., Activity in Emerging Flux Region NOAA 8844 – Flare Genesis Experiment Observations, Solar Group Colloquium, Naval Research Laboratory, Washington, DC, February 13, 2002.

Rust, D. M., Activity in Emerging Flux Region NOAA 8844 – Flare Genesis Experiment Observations, Solar Group Colloquium, NASA Goddard Space Flight Center, Greenbelt, MD, February 27, 2002.

Schmieder B., Aulanier G., Rust D.M, Bernasconi P.N., and Georgoulis M.K., Vector Field Observations of Flux Tube Emergence, Euroconference and IAU Colloquium 188 on Magnetic Coupling of the Solar Atmosphere, June 11 – 15, 2002, Santorini, Greece.

Georgoulis, M. K., Rust, D. M., Bernasconi, P. N., and Schmieder, B., Ellerman Bombs and Low-Lying Activity in an Emerging Flux Region, Euroconference and IAU Colloquium 188 on Magnetic Coupling of the Solar Atmosphere, June 11 – 15, 2002, Santorini, Greece.